Ore Geology Reviews 146 (2022) 104925

Contents lists available at ScienceDirect

Ore Geology Reviews

journal homepage: www.elsevier.com/locate/oregeorev

The hydrothermal footprint of the Crixás deposit: New vectors for orogenic gold exploration in central Brazil

Luana Machado Campos [a,*], Catarina Labouré Bemfica Toledo [a], Adalene Moreira Silva [a], Diego Fernando Ducart [b], Bruno Araújo dos Santos [c], Marcelo Pereira Campos [c], Caio César Aguiar Borges [a]

[a] Institute of Geosciences, University of Brasília, Brasília 70910-900, Brazil
[b] Institute of Geosciences, State University of Campinas, Brasil, R. Carlos Gomes, 250, Campinas, São Paulo 13083-855, Brazil
[c] AngloGold Ashanti Ltd., Rodovia GO-336, 97000 Km 97, Crixás, Goiás 76510-000, Brasil

ARTICLE INFO

Keywords:
Hydrothermal footprint
Orogenic gold deposit
Exploration targeting
Reflectance spectroscopy
Petrophysics
Lithogeochemistry

ABSTRACT

The main gold deposits of the Archaean-Paleoproterozoic Terrain of Goiás, in central Brazil, occur in the Crixás Greenstone Belt, one of the five volcanosedimentary sequences of this terrain. The Crixás orogenic gold deposit consists of several orebodies structurally controlled by low to moderate angle thrust faults, hosted in different stratigraphic units that exhibit contrasting mineralization styles and hydrothermal alteration assemblages.

This study characterizes the hydrothermal footprints of the Palmeiras Structure and Structure IV, which control the orebodies hosted in the hydrothermally-altered mafic metavolcanic rocks and carbonaceous schists, respectively. We assessed the magnitude of fluid-rock interactions by integrating mineralogical, geochemical, and petrophysical data with the reflectance spectroscopy results for drill core samples for both structures.

The Palmeiras Structure hydrothermal footprint is characterized by a distal halo composed of Fe-Mg chlorite + biotite ± carbonates (calcite and Fe dolomite), followed by the intermediate halo defined by epidote + carbonates (dolomite, Fe dolomite, and ankerite) ± Fe-Mg chlorite, and proximal halo composed of muscovite + Fe-enriched chlorite ± paragonite, magnetite, tourmaline, Fe dolomite, and ankerite. Additionally, the chemical pattern of the hydrothermal alteration along the Palmeiras Structure has significantly increased concentrations of alkali (K_2O, Na_2O, Rb, Cs, Li, and Ba), as well as Fe_2O_3, Al_2O_3, TiO_2, LOI, U, W, Th, and Ta towards the gold mineralization. Also, the high magnetite concentration resulted in high magnetic susceptibility and density, with values above 1432.00×10^{-3} SI. In Structure IV, the proximal alteration assemblage comprises muscovite + Fe dolomite, Fe-Mg chlorite + arsenopyrite. The lithogeochemical signature is characterized by enrichment in SiO_2, CaO, Na_2O, K_2O, P, Ba, and pathfinder elements As, W, Sb, Te, that increase towards the gold mineralization. A new potential target hosted in the hydrothermalized metabasalt was identified, whose signature is defined by the occurrence of muscovite, chlorite and enrichment in K_2O, Ba, Rb, Li Cs and pathfinder elements such as As, W, Sb, Te.

This study demonstrates that the integrated application of reflectance spectroscopy, petrophysics and chemical analyses provide a powerful tool for characterizing the hydrothermal footprint and determining the vectors toward gold mineralization in regional-scale mineral exploration.

1. Introduction

The Crixás greenstone belt (CGB), located in the western portion of the Brasilia Belt, is a part of the Archean-Paleoproterozoic Terrain of Goiás (APTG), Central Brazil (Fig. 1). This terrain comprises orthogneiss complexes and metavolcanosedimentary sequences that host significant orogenic gold deposits (e.g. Crixás, Sertão, and Pilar deposits – Jost and Fortes, 2001; Bogossian et al., 2020; Bacha et al., 2021). The CGB hosts the main deposits, where mineralization is controlled by regional-scale shear zones and thrust faults with associated hydrothermal alteration (Thomson and Fyfe, 1990; Jost et al., 2001; Jost et al., 2010).

Orogenic gold deposits are defined as structurally controlled epigenetic deposits, associated with the percolation of hydrothermal fluids during orogenic processes (Goldfarb et al., 2005; Phillips and Powell,

* Corresponding author.

https://doi.org/10.1016/j.oregeorev.2022.104925
Received 19 September 2021; Received in revised form 24 March 2022; Accepted 5 May 2022
Available online 10 May 2022

2010). The percolation of these fluids promotes specifics anomalous and systematic mineralogical and geochemical changes in the host rocks, which the extend and magnitude depend on its deformation state, porosity, permeability, and degree of chemical reactivity (Kishida and Kerrich, 1987; Eilu et al., 2001; Dubé and Gosselin, 2007). These changes generates alteration footprints that may assist in determining the exploratory guides for identifying new high-grade targets in mature mineralized terrains (Eilu et al., 2001; Gaillard et al., 2020). Therefore, characterizing mineralogical and geochemical footprints become extremely relevant in the exploration of orogenic deposits (Eilu and Mikucki, 1998; Large et al., 2000).

The hydrothermal footprint of mineral deposits is assessed by integrating different analytical tools and techniques. Due to its ability to delineate and characterize the alteration patterns, reflectance spectroscopy has been successfully used in exploration targeting for different types of hydrothermal mineral deposits (Ducart et al., 2006; Chang et al., 2011; Harraden et al., 2013; Duuring et al., 2016; Simpson and Christie, 2019, Tian et al., 2019; Zhang et al., 2020a; 2020b). This

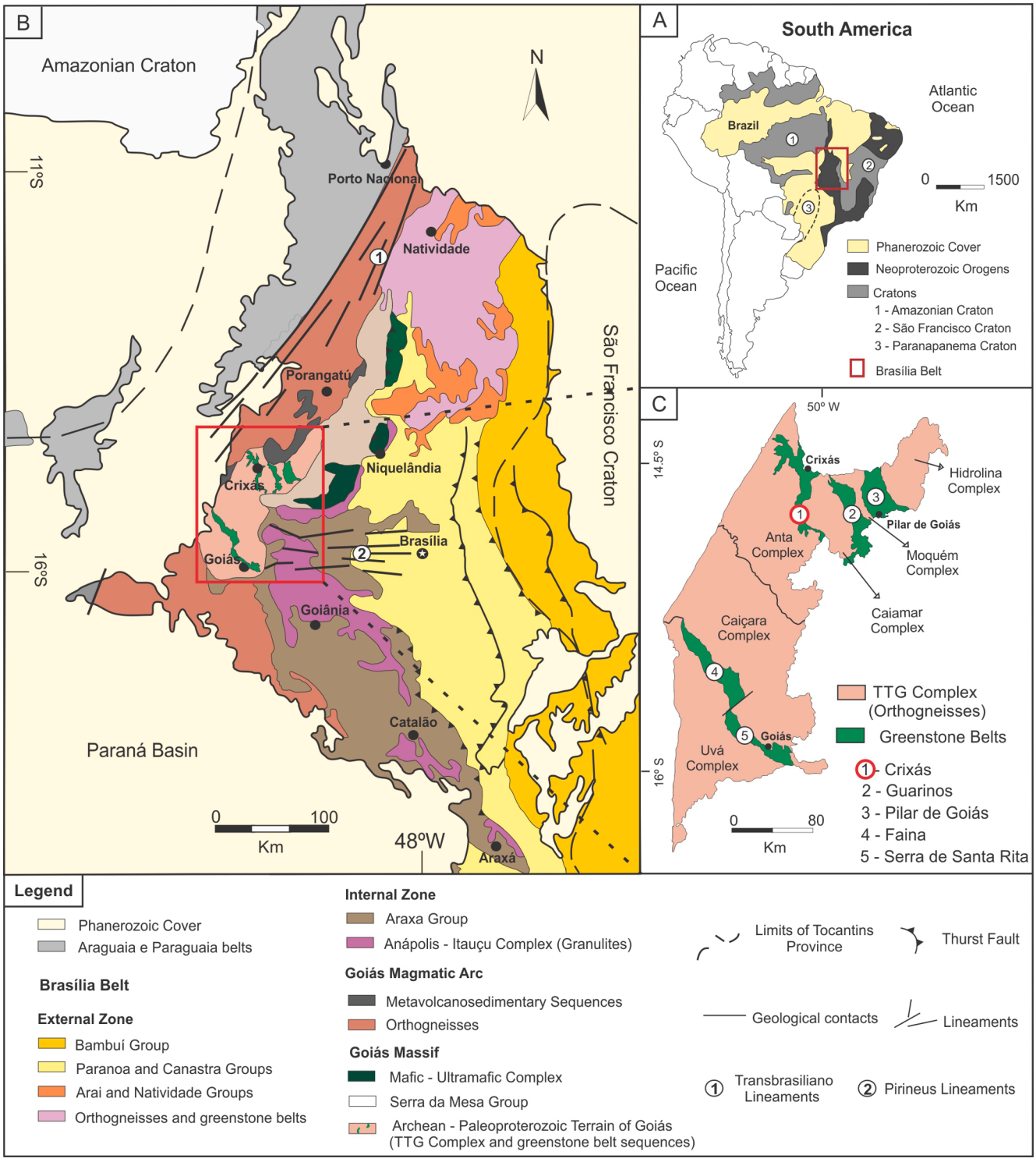

Fig. 1. A) Brazilian geotectonic map. B) Simplified map of the Brasilia Belt showing the main geological units (modified after Pimentel et al., 2004). C) TTGs and greenstonee belts of Archean-Paleoproterozoic Terrain of Goiás. (modified from Jost et al., 2014).

technique allows defining the quantitative and qualitative mineralogical informations, such as relative abundance, chemical composition, and varying crystallinity of some minerals (Van der Meer, 2004), thus helping to delineate and characterize mineralized zones and their hydrothermal alteration halos.

The geochemical footprint can be mapped several hundred meters (>200 m) beyond the economically viable portion of the deposit (Heath and Campbell, 2004). Metamorphic processes taking place in hydrothermal alteration halos associated with orogenic gold deposits are defined by varying degrees of alkali enrichment and pathfinder elements, including As, Hg, Mo, Sb, Se, Te, Ag, and W (Groves et al., 1998; Dubé and Gosselin, 2007; Pirajno, 2009). Mineralogical halos replace the metamorphic mineral assemblages with hydrothermal assemblages associated with sulfidation, carbonation, sericitization, and chloritization processes (Christie and Brathwaite, 2003).

Hydrothermal mineralization processes may produce geophysical anomalies in the host rocks that help to delineate and characterize the associated ore deposits. Given that its geophysical signature is directly related to the chemical, mineralogical and textural changes caused by the alteration processes, the study of physical properties of rocks is fundamental for determining the hydrothermal footprints of ore deposits (Chopping and van der Wielen, 2011; Dentith and Mudge, 2014; Dentith et al., 2020).

In this work, petrographic, reflectance spectroscopy, geochemistry and petrophysics data were integrated to characterize the hydrothermal footprint of the CGB gold deposit and provide guidelines for gold exploration in the Archean-Paleoproterozoic terrain of Goiás. The study was performed in a 1200 m deep drill hole located in the Corpo IV orebody, one of the several orebodies of the CGB.

2. Geological setting

The Tocantins Province, in central Brazil, is a Neoproterozoic (Brazilian-Pan-African) orogenic system derived from the convergence of three continental blocks: Amazonian, São Francisco – Congo, and Paranapanema cratons (Fig. 1; de Almeida et al., 1981), and consists of three fold belts: Araguaia Belt in the northern domain, Paraguay Belt in the southwestern domain, and Brasília Belt, west of the São Francisco Craton (Fig. 1a; Pimentel et al., 2000).

The Brasília Belt is divided into the NE-SW-trending north segment and the NW-SE-trending south segment (Fig. 1a), separated by the Pirineus Syntaxis, which marks the changing structural directions. This belt is divided into External and Internal Zones (Fig. 1a; Araújo Filho, 2000). The External Zone consists of metasedimentary rocks (Bambuí, Paranoá, and Canastra groups), deposited on a passive continental margin structured in a thrust-fold system verging towards the São Francisco Craton (Fig. 1a; Pimentel et al., 2004a; Valeriano et al., 2008). In the northern portion of the External Zone, the Paleoproterozoic basement consists of granites, orthogneisses, and sedimentary sequences represented by the Araí and Nativity groups (Pimentel et al., 2004; Valeriano et al., 2008).

The Internal Zone is subdivided into three main compartments. First, the Goiás Massif comprises the Archean-Paleoproterozoic Terrain of Goiás (Jost et al., 2013), the Paleo-Mesoproterozoic Serra da Mesa metasedimentary rocks, and three Meso-Neoproterozoic mafic-ultramafic layered complexes (Fig. 1a; Ferreira Filho et al., 1994; Ferreira Filho et al., 1998; Pimentel et al., 2004b). Second, the high-grade Anápolis-Itauçu metamorphic core and the Uruaçu complex (Piuzana et al., 2003; Della Giustina et al., 2009), both composed of metasedimentary rocks of the Araxá Group (Seer et al., 2001) and ophiolitic fragments (Fig. 1a; Strieder and Nilson, 1992). Lastly, the Neoproterozoic Goiás Magmatic Arc (Fig. 1a) consists of orthogneisses and metavulcanosedimentary sequences interpreted as a juvenile continental crust generated during the Brasiliano/Pan-African cycle from 900 to 630 Ma (Pimentel and Fuck, 1992).

2.1. The Archean-Paleoproterozoic Terrain of goias

The APTG extends over 18.000 km^2 in the western limit of the Brasília Belt (Fig. 1a) and comprises granite-gneiss complexes of mostly TTG (tonalite, trondhjemite, and granodiorite) composition, as well as remnants of greenstone belt terrains (Fig. 1b).

About 80% of the APTG consists of six individual granite-gneiss complexes with distinct structural, lithological, and geochronological frameworks: the Anta, Caiamar, Moquém, and Hidrolina complexes to the north, and the Caiçara and Uvá complexes to the south (Fig. 1b). Two stages of magmatism were established in the northern complexes (Queiroz et al., 2008). The first stage is recorded in the TTG gneisses of the Caiamar and Anta complexes, with U-Pb zircon crystallization ages between 2845 and 2785 Ma and εNd varying from −1.0 to +2.41 (Queiroz et al., 2008). Magma contamination with older sialic crust was evidenced by inherited zircon crystals with ages between 3.3 and 3.15 Ga (Queiroz et al., 2008). In the Moquém Complex, the second stage is defined by granodiorite and granite intrusions with U-Pb zircon crystallization ages between 2711 and 2707 Ma (Queiroz et al., 2008).

In the southern APTG, the Caiçara Complex consists of tonalitic orthogneisses with a U-Pb zircon crystallization age of 3.14 Ga (Beghelli Junior, 2012). Jost et al. (2013) defined two groups of orthogneisses in the Uvá Complex. The first group consists of polydeformed tonalitic and granodioritic batholiths and a diorite stock. Tonalite U-Pb ages were constrained between 3040 and 2930 Ma while zircon U-Pb dating of diorite showed the age of 2934 ± 5 (Pimentel et al., 2003; Jost et al., 2013). The second group is defined by smaller, tabular, and isotropic tonalite and monzogranite bodies with U-Pb zircon dating between 2764 and 2846 Ma (Jost et al., 2013).

The supracrustal sequences comprise about 20% of the APTG and are represented by five elongated metavolcanosedimentary sequences confined between the TTG complexes (Danni and Ribeiro, 1978). The Crixás, Guarinos, and Pilar de Goiás greenstone belts occur to the north (Fig. 1b). The Faina and Serra de Santa Rita greenstone belts occur to the south, juxtaposed by a dextral strike-slip fault (Fig. 1b). The stratigraphic sequences of the five greenstone belts consist of metavolcanic sequences formed by komatiites and metabasalts overlapped by metasedimentary sequences with particular characteristics in each greenstone belt. These rocks underwent polycyclic deformation and greenschist to lower amphibolite facies metamorphism (Jost et al., 2014).

The APTG origin and its role in the evolution of the Brasilia Belt have been much debated. Some authors interpret it as an allochthonous Archean-Paleoproterozoic microcontinent amalgamated to the Brasilia Belt during the Neoproterozoic Brasiliano Orogeny (Pimentel et al., 2000; Jost et al., 2013). On the other hand, recent studies suggest that the APTG and the other tectonic domains of the Goiás Massif are part of a continuous continental mass of the São Francisco-Congo paleocontinent that was already amalgamated since the late Paleoproterozoic (de Oliveira Cordeiro and de Oliveira, 2017; Borges et al., 2021a).

2.2. The crixás greenstone belt

The CGB extends 6 km wide and is approximately 45 km long in the northern portion of the APTG. It is bordered by the Caiamar Complex to the east, the Anta Complex to the west, and the Neoproterozoic metasedimentary rocks of the Santa Terezinha Sequence to the north (Fig. 2a).

2.2.1. Stratigraphy

The CGB stratigraphic sequence is defined by a lower ultramafic-mafic metavolcanic sequence, represented mainly by metakomatiites and ultramafic schists, as well as tholeiitic metabasalts and mafic schists (Fig. 2a; Sabóia and Teixeira, 1983); and an upper metasedimentary sequence, composed of a thick layer of carbonaceous schists with dolomite lenses that gradually transition to metagraywackes at the top

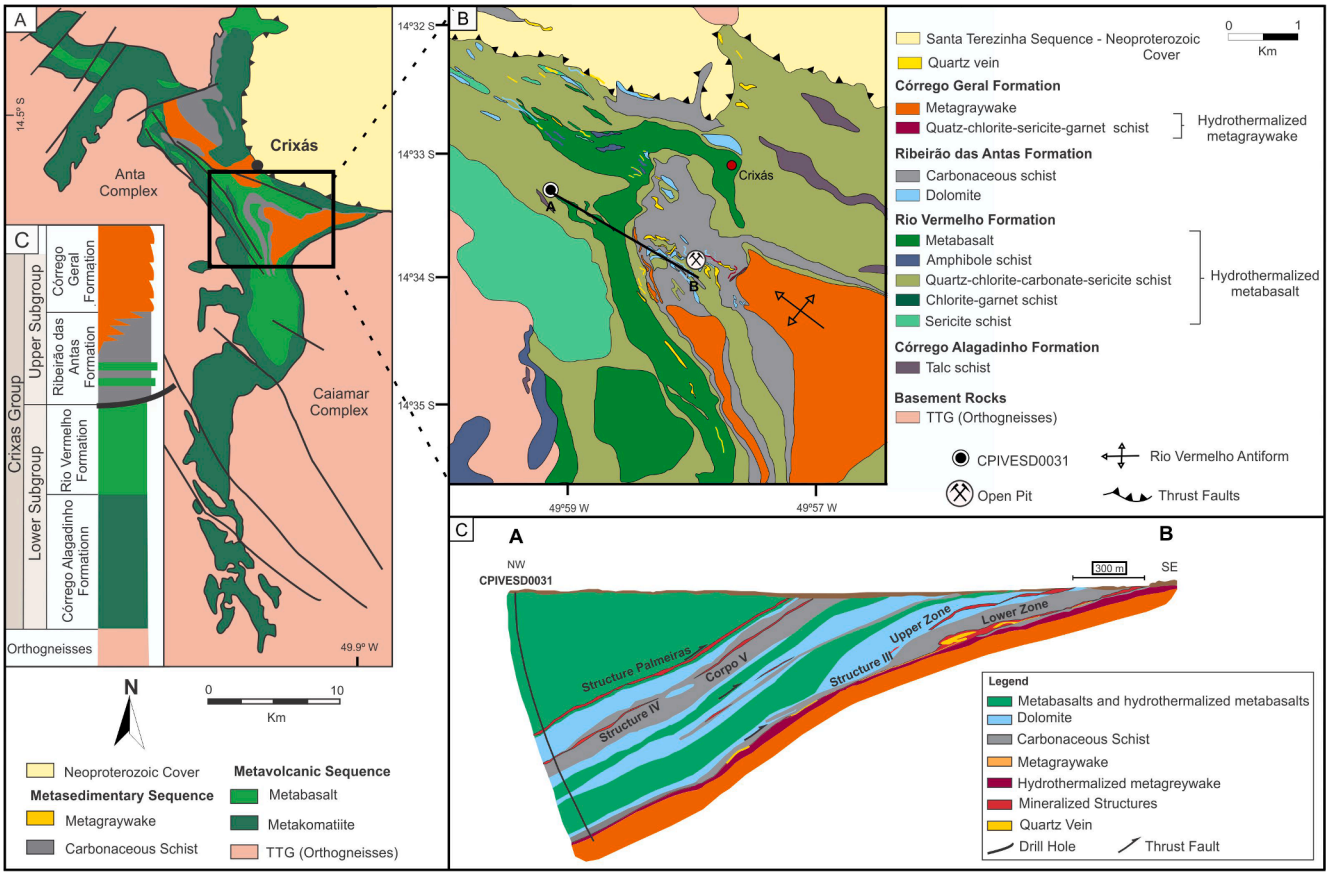

Fig. 2. A) Geological map and Stratigraphic column of the Crixás greenstone belt (modified from Jost et al., 2014; Jost et al., 2019). B) Lithological map of Crixás greenstone belt showing the location of the CPIVESD0031 drill hole and the section of Corpo IV (provided by AngloGold Ashanti – unpublished data). C) Geological section of Corpo IV exhibiting the mineralized structures (provided by AngloGold Ashanti – unpublished data). The older Archean metavolcanic rocks are overlapped the Rhyacian metasedimentary sequence.

of the sequence, composing a turbiditic succession (Fig. 2a; Jost and De Oliveira, 1991; Jost et al., 1996; Jost et al., 2019).

In low-stress zones, the metavolcanic rocks are locally preserved and exhibit primary textures such as olivine cumulates, polyhedral disjunctions, spinifex textures, pillow lavas, amygdalas, and vesicles (Kuyumjian, 1981). Thin layers of banded iron formations, gondite, and metacherts are interspersed with the volcanic rocks (Kuyumjian, 1981). Geochronological studies in metakomatiites and metabasalt samples provide Sm-Nd and Pb-Pb errochrons of ca. 3.0 and 2.8 Ga (Arndt et al., 1989; Fortes et al., 2003). Recently, Borges et al. (2021b) obtained a Re-Os isochron of 2609 ± 65 Ma, interpreted as a metasomatic event related to the emplacement of the youngest Archean granites of the region (ca. 2.7 Ga) that overprinted the regional Re-Os isotopic signature of the rocks. In summary, current data indicates that the protoliths are of the Archean age.

Isotopic data of the metasedimentary sequence indicates Archean to Rhyacian ages (Resende et al., 1998; Fortes et al., 2003; Tassinari et al., 2006; Jost et al., 2008; Jost et al., 2014; Jost et al., 2019; Borges et al., 2021a). Detrital zircon U-Pb ages of metagreywacke and carbonaceous schist samples show a dominant source dated ca. 2.2 – 2.1 Ga, with a minor contribution from sources dated ca. 2.7–2.4 Ga (Jost et al., 2008; Borges et al., 2021a). The youngest zircon crystals provided a maximum deposition age of 2149 ± 2 Ma (Borges et al., 2021a). The rocks present relatively homogeneous Sm-Nd model ages (2.5 to 2.34 Ga) and ƐNd (-0.27 to + 1.25) (Borges et al., 2021a). Intermediate magmatism associated with the metasedimentary sequence of the CGB was dated 2172 ± 13 Ma (Borges et al., 2021b).

2.2.2. *Deformation and metamorphism*

The CGB deformational evolution comprises four major compressive events (Magalhães, 1991; Queiroz, 1995; Queiroz, 2000; Massucato, 2004). The first event generated regional-scale isoclinal folds with axial foliation parallel to the original bedding, under low- to moderate-grade metamorphic conditions (Massucato, 2004). The second event is characterized by an E-W progressive compression that generated shear zones and low-angle thrust faults associated with semi-recumbent folds and was responsible for the inversion of the stratigraphic sequence (Magalhães, 1991; Queiroz,1995), and favored the percolation of the hydrothermal fluids, responsible for the gold concentration and deposition in the region (Massucato, 2004). The third event is related to an N-S compression that generated the partial overlapping of the Mara Rosa Arch to the north and generated the Rio Vermelho Antiform (Fig. 2b; Magalhães, 1991). The folding caused partial remobilization of gold, which concentrated parallel to the axial axes of the folds and defined the mineralization plunge. Late NNW-SSE compression produced crenulations and smaller folds (Massucato, 2004).

Because the CGB rocks underwent greenschist to amphibolite facies metamorphism, the stratigraphic reconstruction is complex due to the polycyclic deformation, thickening, and the rarity of marker horizons (Jost et al., 2014).

2.2.3. *Gold mineralization*

The CGB gold exploration began in the 18th century by the Bandeirantes. In the 70s, the first regional prospective research by the joint venture between the Inco and Kennecott partners discovered the giant Mina III orebody. Mineração Serra Grande, which currently belongs to AngloGold Ashanti, started the gold production in the late 80s and as the

exploratory programs extended over the years, several exploration targets have been continuously discovered in the Crixás deposit. According to recent technical reports, the Crixás gold deposit has a mineral resource of approximately 3.69 Moz, with an annual production of 114–123 Koz and gold grade up to 8 g/t (https://www.anglogoldashanti.com/portfolio/americas/serra-grande, accessed on March, 23, 2022).

Studies define an epigenetic model for the Crixás gold deposit, which would be generated from a late-metamorphic hydrothermal event associated with shear zones (Thomson, 1987; Fortes, 1996; Portoccarrero, 1996). The mineralization is hosted in metasedimentary and metabasalt rocks, with differing mineralogical assemblages and hydrothermal alteration degrees. It occurs as: (i) massive sulfides, (ii) quartz veins, and (iii) disseminated ore (Jost and de Oliveira, 2001; Jost et al., 2010). The mineralized zones were developed in dilation zones controlled by second-order thrust faults related to stacked major low- to moderate-angle detachment faults and semi-recumbent folds (Thompson, 1987; Jost et al., 2001; Ulrich et al., 2021). The main structures controlling the several orebodies of the Crixás gold deposit are Palmeiras Structure, Structure IV, and Structure III. The orebodies exhibit linear shapes with shallow plunge and continuity along the NW to W-WNW trending structures (Ulrich et al., 2021).

The Palmeiras Structure controls the gold mineralization in the Palmeiras, Palmeiras Norte, and Baru orebodies. This low-angle shear zone intercepts the hydrothermally-altered mafic metavolcanic next to the contact with a dolomitic layer (Fig. 2c). The mineralization occurs in quartz veins or as disseminated ore associated with pyrite and in fractures in magnetite crystals.

Structure IV is a low-angle shear zone that intercepts the carbonaceous schists (Fig. 2c) and controls the mineralization in the Corpo IV, Corpo V, Corpo Forquilha, Corpo Pequizão, Corpo Mangaba, and Corpo Sucupira orebodies. The gold mineralization occurs in intense silicification zones and is associated with quartz veins and/or disseminated as gold-rich arsenopyrite and pyrrhotite.

Structure III controls the mineralization in the Mina III, Mina Nova, Corpo IX, Inga, and other orebodies, is divided into Upper and Lower Zones and also occurs in the hydrothermally-altered carbonaceous schist of the Ribeirão das Antas formation. The Upper Zone (Yamaoka & Araújo, 1988) is related to massive sulfides lenses composed mainly of arsenopyrite and pyrrhotite. The Lower Zone is a low-angle thrust fault in the carbonaceous schist above the contact between the metagraywacke. Its mineralization is related to arsenopyrite, pyrrhotite and minor chalcopyrite disseminated in 0.5 to 5 m thick quartz veins that reach up to 700 m deep.

The first geochronological studies on the hydrothermal alteration halos applying Rb-Sr, K-Ar, and Ar-Ar methods determined mineralization ages from 750 to 550 Ma, suggesting that the Crixás gold mineralization is Neoproterozoic and related to the Brasiliano Orogeny (Fortes, 1996; Fortes et al.,1997). Later Re-Os dating in arsenopyrite from massive sulfide lenses of the Mine III Upper Zone indicates dates ca. 2126 ± 16 Ma (Marques et al., 2013), and 2137 ± 11 Ma (Borges et al., 2021b), suggesting a Paleoproterozoic age for the mineralization and indicating that the previously obtained Neoproterozoic age likely represents the metamorphic overprinting due to the Brasília Belt Orogeny (Jost et al., 2014).

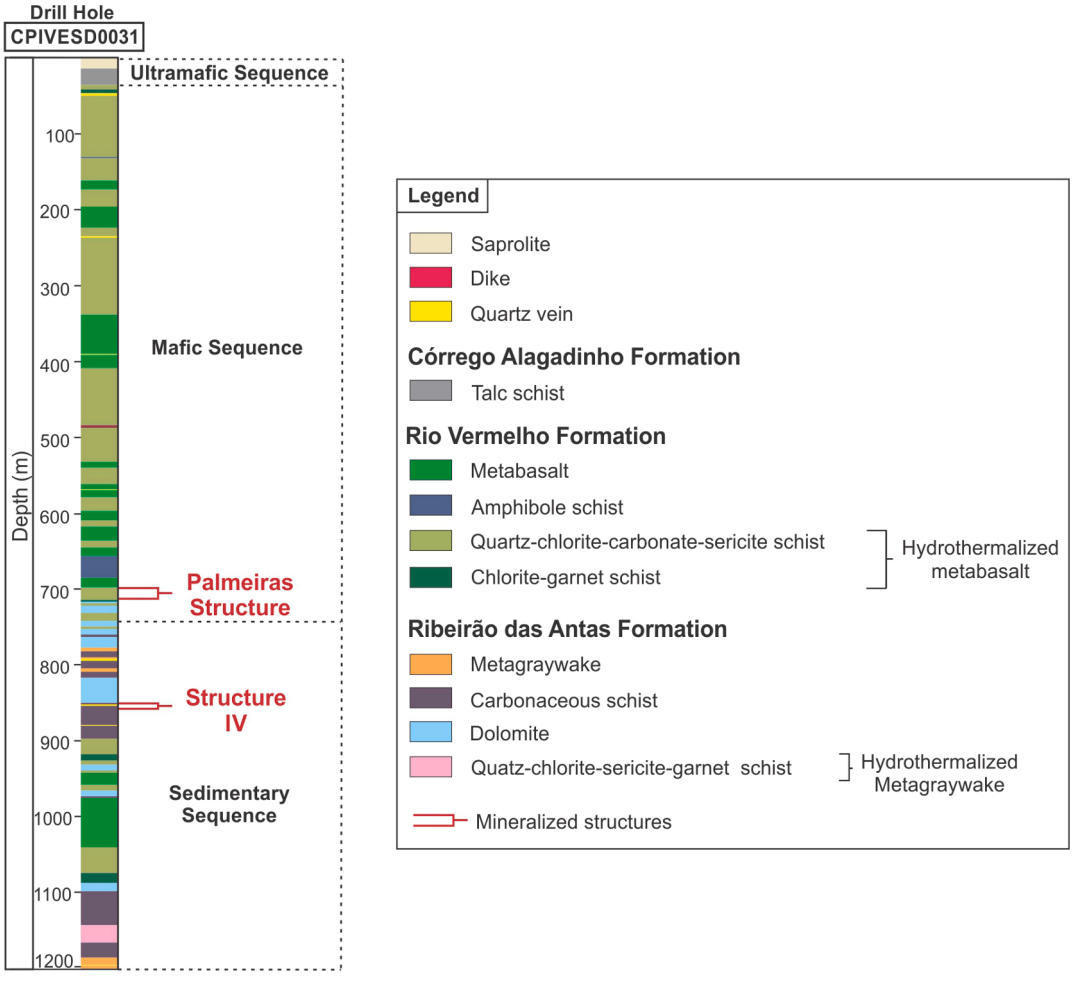

Fig. 3. Log profile of the drill hole CPIVESD0031 illustrating the mineralized Palmeiras Structure and Structure IV.

3. Sampling and analytical methods

3.1. Sampling

This study focuses on the Palmeiras Structure and Structure IV that intercept the metabasalts and carbonaceous schists, respectively (Fig. 3). The sampling was performed in drill core samples collected from a 1200 m deep drill hole located in the Corpo IV orebody (Fig. 3). Fifteen cm-long core samples were collected from the CPIVESD0031 drill hole every 2 m, with denser sampling (i.e., every 1 m) in the mineralized zones. A total of 619 samples were used for the petrographical, spectral, geochemical, and petrophysical investigation.

3.2. Petrography and mineral chemistry

A total of 30 representative thin sections were petrographically analyzed to identify the mineral assemblages as well as the metamorphic and hydrothermal textures recorded on host rocks and mineralized samples. Also, mineral chemistry analyses were performed at the Electronic Microprobe Laboratory of the University of Brasilia to complement the petrographical study. The JEOL JXA-8230 equipment used works between 15 and 20 kV, 10 to 20nA current, and 1 to 5 μm beam diameter. The analyzed minerals include chlorite, amphibole, carbonates, micas, and plagioclases. The analytical results are included in the supplementary data (Appendix C).

3.3. Reflectance spectroscopy

Reflectance spectroscopy data were obtained with a FieldSpec-3 HiRes® spectroradiometer (ASD). The instrument works within a 350–2500 nm spectral range and a 1.4 nm to 350–1050 nm (VNIR) and 2 nm to 1000–2500 nm (SWIR) sampling interval, with a spectral resolution of 3 nm on VNIR and 8 nm on SWIR. Each saved spectrum represents the average of 50 spectra measured at the same points and in total 5457 spectra were acquired in 607 samples. The spectral signatures were analyzed using The Spectral Geologist (TSG CoreTM) software.

Each mineral has a specific spectral signature, controlled by its chemical composition and crystal structure, wich is defined by the spectral parameters position, shape, and depth of the absorption features (Van der Meer, 2004). The relative abundance, chemical composition, and degree of crystallinity data are acquired based on the spectral parameters calculations that can be directly correlated with other numeric attributes such as geochemistry. In this study, the relative abundance and chemical composition of each mineral was obtained by the depth and the wavelength position of the deepest absorption feature in the continuum-removed spectrum, respectively. Filters and masks adapted for this work to obtain the spectral indices are presented in Appendix A.

The spectral parameter calculations results were plotted in a schematic profile of the drill hole CPIVESD0031 to understand the varying spectral properties of some key minerals concerning the different lithological and alteration patterns along the drill core. The results were validated by the petrographical and mineral chemistry analyses.

3.4. Geochemistry

Whole-rock geochemical analyses of 619 samples were performed following standard laboratory procedures at the commercial geochemistry ALS Laboratory, in Goiânia, Brazil. Major elements are presented as the weight percentage of elemental oxide determined by the ICP – AES method. Trace elements, including rare earth elements (REE), are presented as a percentage per million (ppm) determined by ICP-MS. C and S dosages were determined by the combustion furnace method. The metals Ag, As, Cd, Cu, Li, Mo, Ni, Pb, Sc, Tl, and Zn were determined by ICP-AES. It is highlighted that the iron analysis corresponds to Fe2O3T. A complete description of the analytical methods and the CCP-PKG01 package is available on the ALS website (www.alsglobal.com). The analytical results are included in the supplementary data (Appendix D). Elements present in amounts below the detection limit of the methods are not shown in the tables. Geochemical data were processed using Excel (Microsoft).

To characterize the geochemical patterns of mineralized structures, strip logs were constructed with chemical analysis for major and minor elements from the drill core samples. These profiles allowed us to assess the chemical behavior of elements throughout the CPIVESD0031 drill hole. To compare the geochemical signatures of the hydrothermalized halos and host rocks, the ratios between the dosages of chemical elements in the hydrothermalized and non-hydrothermalized samples were calculated for each mineralized zone. Ratios above 1 indicate that the element concentration increased in the alteration halo relative to the unaltered sample, while ratios below 1 indicate depletion.

3.5. Petrophysics

Density and magnetic susceptibility were determined to characterize the physical properties signatures of the lithological units and the mineralized structures of the CGB. The results of the density calculations and magnetic susceptibility measurements versus CPIVESD0031 drill hole depth were plotted in scatter plots. Table 1 and box plots show the statistical analysis results.

The density of drill core samples was determined by weighing 607 samples in an IND560 industrial weighing scale. A docked base was used to weigh the samples immersed in water. The density values were calculated based on the Archimedes Principle, which determines that: Ds = (Mss/Mss-Msi). Dl, where Ds is the density of a solid; Mss is the dry solid mass; Msi, wet solid mass, and DI is the density of the liquid used in the measurements.

The magnetic susceptibility was measured using a portable KT-10 susceptibility meter, manufactured by Terra Plus. This equipment

Table 1
Magnetic susceptibility and density of the CGB rock units measured in the CPIVESD0031 drill hole samples.

Lithology		Magnetic Susceptibility (x 10–3SI)	Density (g/cm^3)
Talc schist	Mean	4.491	2.884
	Range	0.428–8,287	2.812 – 2.956
Metabasalt	Mean	0.639	3.009
	Range	0.131 – 2.233	2.786 – 3.67
Quartz-chlorite-carbonate-sericite schist	Mean	0.707	2,876
	Range	0.204 – 1424.545	2.5 – 3.576
(densdade e susceptibilidade magnética) Chlorite-garnet schist	Mean	0.838	2.879
	Range	0.355 – 75.632	2.428 – 3.727
Amphibole schist	Mean	0.729	3.080
	Range	0.514 – 0.849	2.875 – 3.2
Dolomite	Mean	0.120	2,825
	Range	0.006 – 0.518	2.130 – 3.733
Carbonaceous schist	Mean	0.421	2,781
	Range	0.020 – 2.876	2.471–3.880
Metagreywacke	Mean	0.385	2,802
	Range	0.137 – 0.642	2.658 – 2.980
Quartz-chlorite-garnet-sericite schist	Mean	0.584	3.030
	Range	0.311 – 2.769	2.933 – 3.165

works in contact with the sample and provides values in $\times 10^{-3}$ SI units. All values are averages of 3 measurements per sample.

4. Results

4.1. Gold mineralization and hydrothermal alteration

Based on petrographic analyses, the observed mineralogical and textural variations allowed the determination of alteration halos from unaltered portions of the host rock to the distal, intermediate and proximal portions of each mineralized zone. The adopted lithotype nomenclature was previously defined by Mineração Serra Grande Ltd and is summarized in Fig. 3.

4.1.1. Palmeiras structure

Compositional and textural variations towards the mineralized zone allowed to differentiate the unaltered metabasalt and the hydrothermal alteration halos, defined as distal, intermediate, and proximal halos (Fig. 5a–e).

4.1.1.1. Metabasalt (Unaltered host rock). The mafic metavolcanic sequence (Rio Vermelho Formation) is characterized by dark green, predominantly fine- to medium-grained massive to slightly foliated metabasalts (Fig. 5a). Locally, primary igneous features like pillow lavas and amygdalas can be observed. The metabasalt metamorphic assemblage consists of hornblende (ca. 30–60 vol%), plagioclase (ca. 10–30 vol%), and carbonate (ca. 3–10 vol%), with subordinate chlorite, actinolite, epidote, and quartz (ca. 1–5 vol%). Ilmenite (ca. 1–3 vol%), titanite, apatite, rutile, and sulfides (pyrite and chalcopyrite) occur as accessory minerals, corresponding to <1 vol% of the modal composition.

The primary texture is pseudomorphic intergranular. The interstices between the euhedral to subhedral amphibole crystals are filled with recrystallized and very fine-grained anhedral plagioclase and quartz (Fig. 5f and g). Fine-grained secondary carbonates may be present. Metamorphic nematoblastic texture domains are marked by the preferential orientation of amphiboles in one or more directions, associated with granoblastic texture domains consisting of recrystallized quartz, plagioclase, and carbonate. Primary amygdalas and late carbonate or quartz-rich veinlets may occur.

Mineral chemistry data (Appendices B and C) indicate that the plagioclase composition corresponds to oligoclase, whereas amphibole has a transitional composition between Mg-hornblende and tschermakite, predominantly. Actinolite may also be present. The hornblende + oligoclase mineral assemblage indicates metamorphism under amphibolite facies. The presence of chlorite, actinolite, and epidote indicates retrograde metamorphism under greenschist facies conditions.

4.1.1.2. Distal hydrothermal alteration halo. The distal halo of the Palmeiras Structure is represented by foliated greenish-gray schist, defined by alternating amphibole- and lamellar minerals-rich domains, and quartz- and carbonate-rich domains (Fig. 5b). It consists of chlorite (ca.

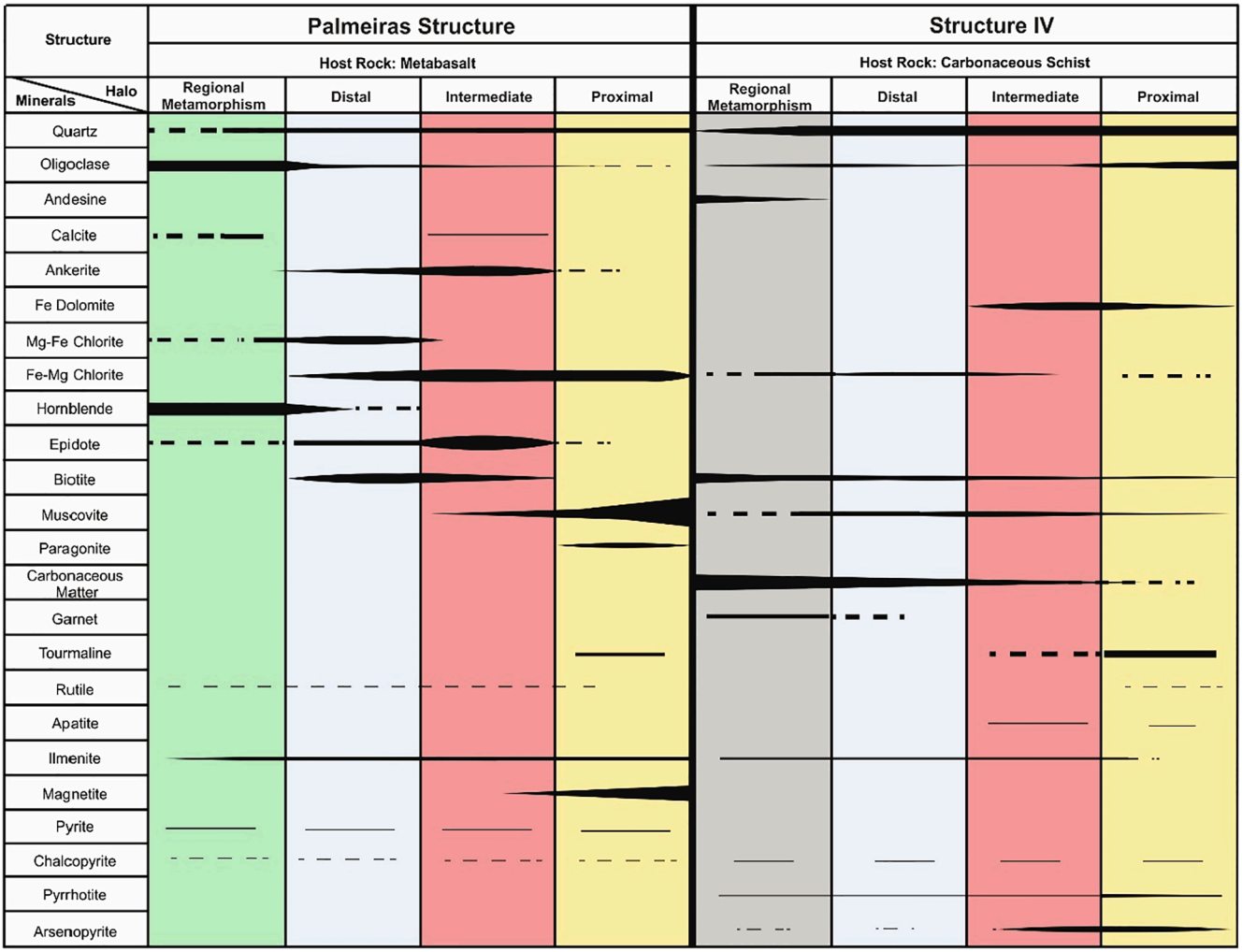

Fig. 4. Paragenetic sequences of the hydrothermal alteration halos of the Palmeiras Structure and Structure IV. The line thickness indicates mineral concentrations.

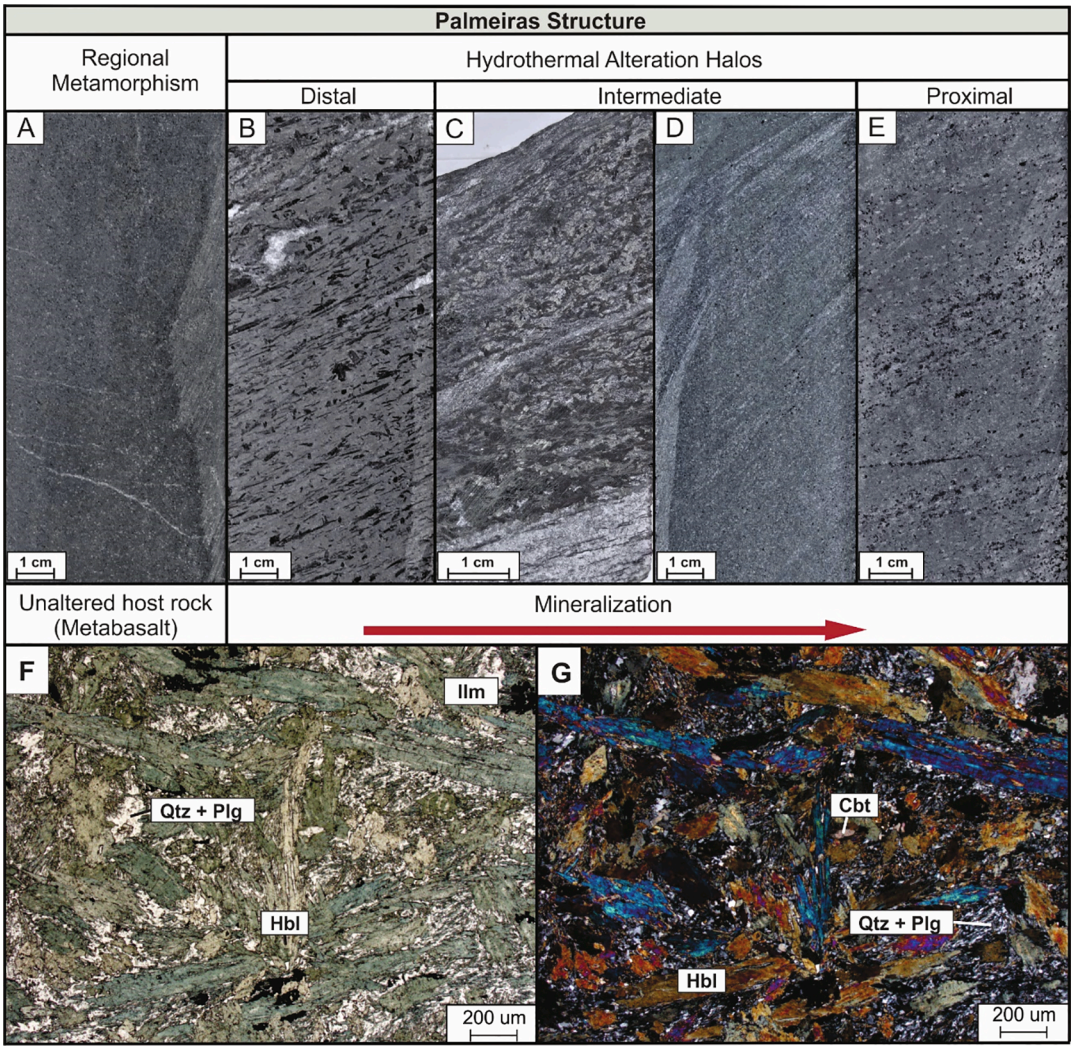

Fig. 5. Samples of the Palmeiras Structure hydrothermal alteration halos. From left to right, unaltered host metabasalt (A), and the distal (B), intermediate (C and D), and proximal halos (E). (F and G) Photomicrographs of fine-grained metabasalt showing partially preserved intergranular texture, characterized by recrystallized plagioclase and quartz in the interstitial spaces between large subhedral hornblende crystals. Images are in plane (F) and crossed polarized lights (G). Abbreviations: Cbt – carbonate; Hbl – hornblende; Ilm – ilmenite; Plg – plagioclase; Qtz – quartz.

15–30 vol%), hornblende (ca. 15–20 vol%), quartz (ca. 20–30 vol%), plagioclase (ca. 10–15 vol%), biotite (ca. 10–15 vol%), carbonate (ca. 1015 vol%), epidote (ca. 2–5%), ilmenite (ca. 1%), sulfides (<1 vol%), and rutile (<1 vol%). The texture is lepidoblastic, marked by chlorite and biotite orientation. Biotite may be partially or totally replaced by chlorite (Fig. 6a). Subhedral hornblende, oriented according to one or two directions of tectonic foliation, defines the nematoblastic texture domains. Fine-grained quartz and plagioclase constitute recrystallized granoblastic domains. Fine-grained anhedral carbonate may occur in minor proportions. Ilmenite is characterized as small fine-grained oriented prismatic subhedral crystals. The sulfides are very fine-grained anhedral pyrite and chalcopyrite. Quartz and carbonate-rich veinlets may also occur.

Mineral chemistry data indicate an oligoclase composition for the plagioclase and compositions ranging from Mg-hornblende to tschermakite for the amphibole. Chlorite has significant Fe content and is classified as ripidolites. Carbonates are classified as calcite and Fe-dolomite (Appendices B and C). The metamorphic paragenesis of amphibolite facies is partially preserved, represented by hornblende and oligoclase. Chlorite, biotite, carbonate, and epidote constitute the hydrothermal assemblage of this halo.

4.1.1.3. Intermediate hydrothermal alteration halo. The intermediate halo exhibits rocks with similar mineralogical composition but different mineral textures and proportions. In general, this halo has a greenish-gray rock, marked by alternating layers of quartz and carbonate with layers of micaceous minerals and epidote porphyroblasts that are oriented according to the tectonic foliation (Fig. 5c and Fig. 6d). A fine-grained gray rock, with a less developed foliation, is also observed in the transition to the proximal halo (Fig. 5d). This transitional domain consists of micaceous minerals, carbonate, quartz, fine-grained magnetite, and less epidote. Veinlets filled with quartz and carbonate are common.

The mineral assemblage consists of chlorite (ca. 30–40 vol%), epidote (ca. 10–30 vol%), carbonate (ca. 15–30 vol%), quartz (ca. 15–40 vol%), biotite (ca. 2–8 vol%), ilmenite (ca. 3 vol%), and sulfides (pyrite and chalcopyrite <1 vol%). Allanite and rutile constitute <1 vol % of the modal composition. Very fine-grained plagioclase (ca. 5–15 vol %) occurs in recrystallized domains and may be saussuritized. Magnetite (<3 vol%) and muscovite (<15 vol%) may also be present. Compared to the distal halo, the main difference is the complete absence of Mg-hornblende and decreasing biotite, giving rise to higher concentrations of epidote and carbonate. Muscovite and magnetite appear in the transition to the proximal halo.

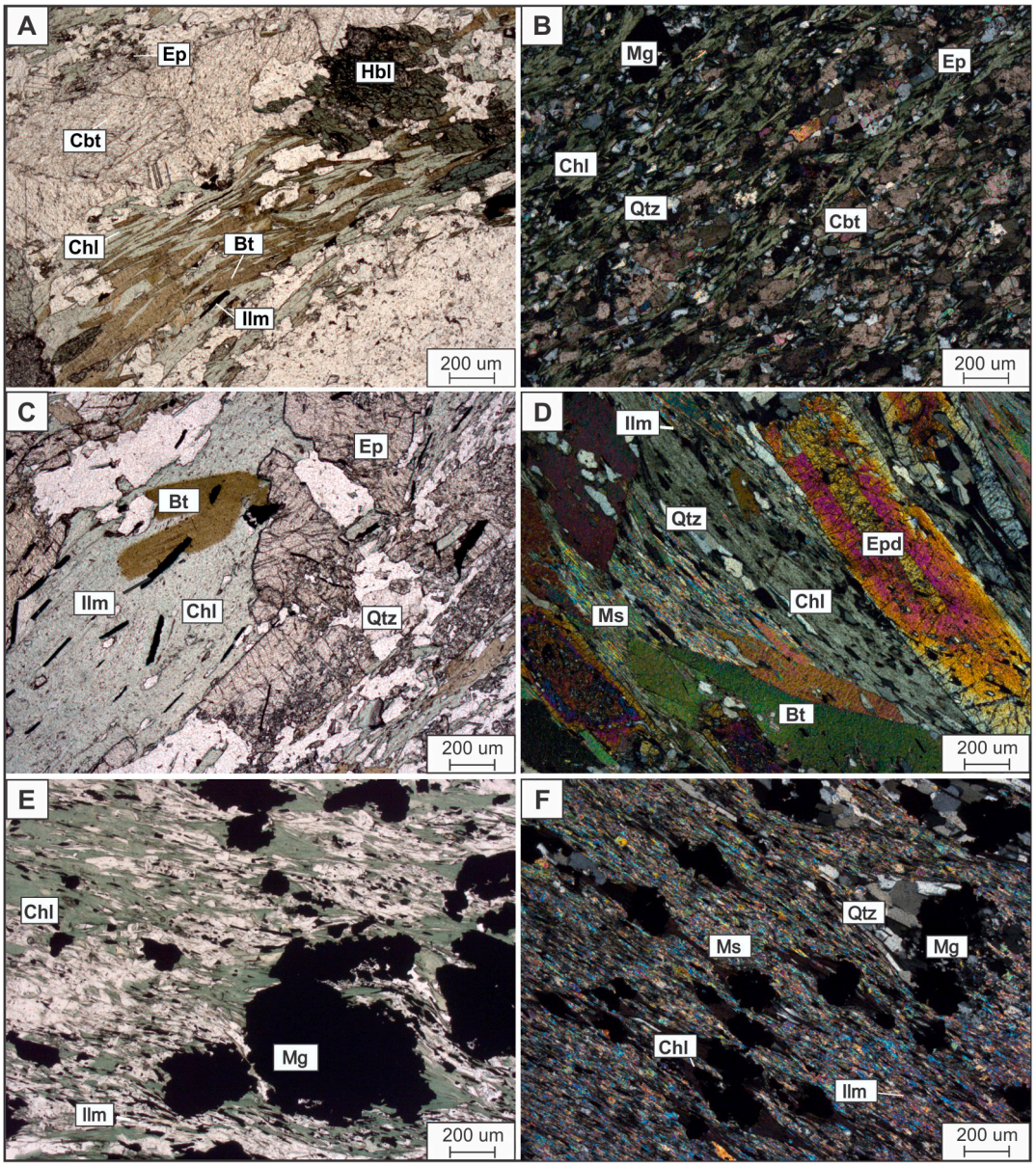

Fig. 6. Photomicrographs of the Palmeiras Structure hydrothermal alteration halos. A) Distal halo: Chlorite replacing biotite oriented according to the foliation. B) Intermediate halo: Lepidoblastic texture is defined by chlorite and granoblastic domains composed of carbonate, quartz, and plagioclase. C and D) Intermediate halo: epidote and biotite porphyroblasts and chlorite oriented according to the tectonic foliation and a muscovite and fine-grained recrystallized quartz-rich groundmass. E and F) Proximal halo: sin- to late-tectonic magnetite porphyroblasts arranged in a matrix consisting of muscovite and paragonite, Fe-Mg chlorite and ilmenite oriented according to the foliation. Abbreviations: Bt – biotite; Cbt – carbonate; Chl – chlorite; Ep – epidote; Hbl – hornblende; Ilm – ilmenite; Mg – magnetite; Ms – muscovite; Qtz – quartz.

This halo is also characterized by a strongly foliated rock with a lepidoblastic texture defined by chlorite, muscovite, and biotite. Biotite porphyroblasts up to 4 mm also occur. Subhedral epidote porphyroblasts up to 1 cm are observed encompassing inclusions of fine-grained oriented ilmenite and minerals of the rock matrix. The epidote can also occur as fine-grained anhedral crystals, defining granoblastic domains with fine-grained quartz and plagioclase (Fig. 6c and d). Carbonate appears as fine to medium-grained anhedral crystals in smaller proportions.

A third petrographical pattern of this transitional domain is defined by a fine-grained grayish rock composed of chlorite and carbonate, predominantly. Quartz, plagioclase, epidote, biotite, ilmenite, magnetite, muscovite, and sulfides occur in minor proportions. The orientation of the chlorite lamellae defines the lepidoblastic texture. Medium-grained anhedral carbonate and fine-grained quartz-enriched portions define the granoblastic texture domains (Fig. 6b). Fine-grained rod-shaped ilmenite occurs oriented according to the foliation. Magnetite appears as fine- to medium-grained subhedral crystals. Fine-grained quartz and plagioclase crystals compose the recrystallized matrix.

Compared with the distal halo, the carbonate composition shows a Fe and Mg increase and Ca decrease, also classified as Fe dolomite and ankerite, while chlorite is classified as ripidolite and exhibits Fe increase and Mg decrease. Plagioclase composition corresponds to oligoclase (Appendices B and C).

4.1.1.4. Proximal hydrothermal alteration halo. The proximal halo is characterized by grayish fine-grained foliated rock, consisting of magnetite and mm-sized quartz-rich domains intercalated with chlorite- and mica-rich layers (Fig. 5e).

The mineral assemblage consists of chlorite (ca. 25–35 vol%),

muscovite (ca. 30–45 vol%), quartz (ca. 15–20 vol%), plagioclase (ca. 10–12 vol%), and magnetite (ca. 10–15 vol%), as well as ilmenite (ca. 3 vol%), epidote (<1 vol%), tourmaline (<1 vol%), and sulfides (<1 vol %), such as pyrite and chalcopyrite. The tectonic foliation is characterized by a spaced, anastomosing schistosity, defined by the preferential orientation of muscovite and chlorite lamellae, among fine-grained recrystallized groundmass of quartz and plagioclase. Quartz is also present as a medium to fine-grained recrystallized crystals in lenses associated with pressure shadows developed around magnetite porphyroblasts (Fig. 6e and f). Ilmenite occurs as rod-shaped crystals oriented according to the foliation. Very fine-grained green tourmaline may be present disseminated in the rock, as well as relics of fine-grained anhedral epidote and carbonate crystals.

This halo differs from the others due to white mica and magnetite enrichment, biotite disappearance, and the restricted occurrence of epidote and carbonate. Compared to the distal and intermediate halos, chlorite and carbonate are more enriched in Fe while plagioclase has an oligoclase composition. White mica predominantly has a muscovite composition and paragonite is also present in minor proportion (Appendices B and C).

4.1.2. *Structure IV*

4.1.2.1. Carbonaceous schist (Unaltered host rock). Structure IV intercepts the carbonaceous schist characterized as a dark, foliated and fine-grained rock composed of thin layers of black carbonaceous matter and micaceous minerals, alternated with thin quartz and plagioclase-bearing layers (Fig. 7a). Disseminated fine-grained sulfide and quartz

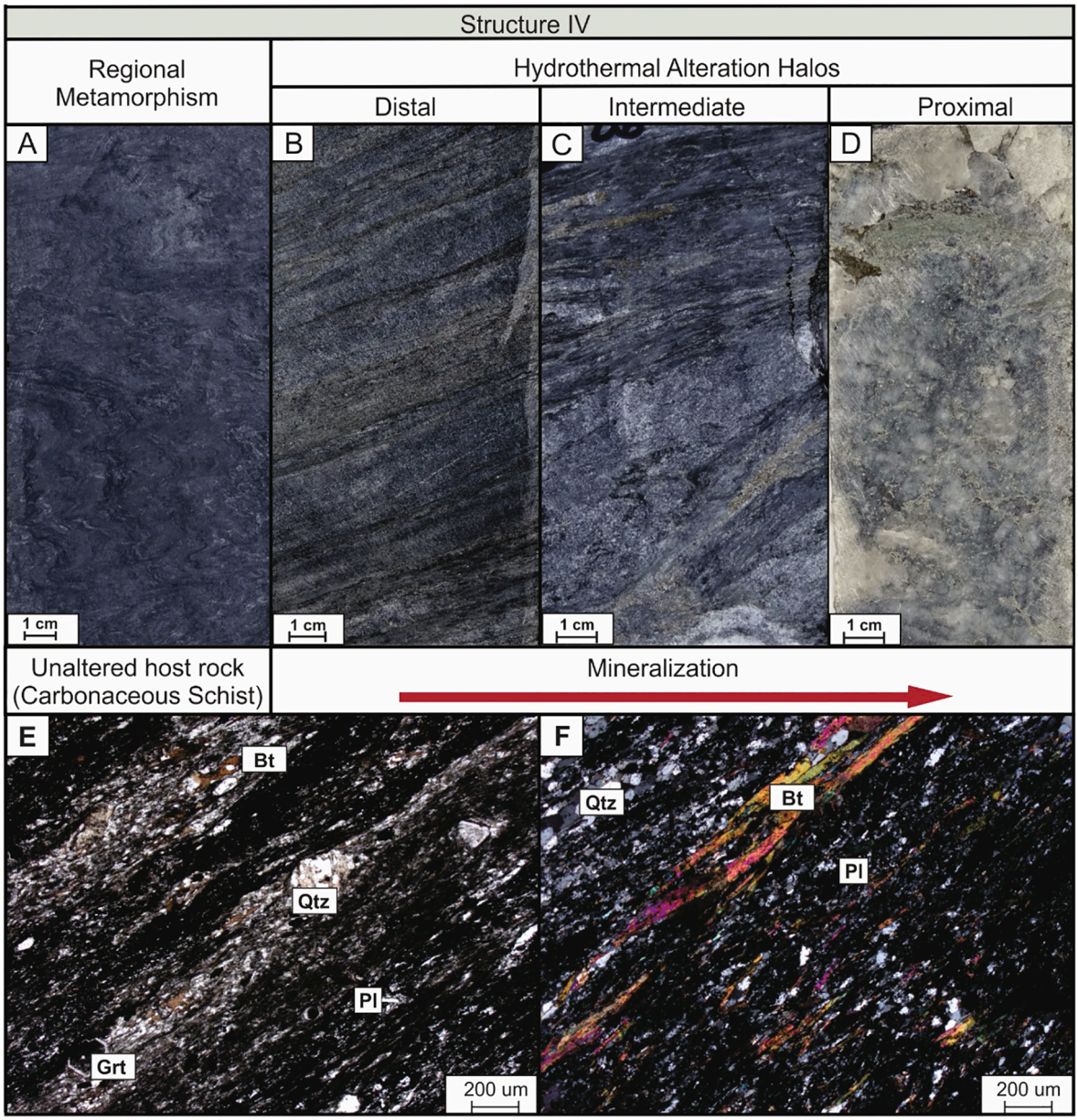

Fig. 7. Samples of Structure IV mineralized zone. A) Fine-grained dark gray carbonaceous schist, with crenulations and partial overprint of S1 foliation. B) Distal halo: fine-grained gray rock, strongly foliated, characterized by alternating carbonaceous matter and micaceous-bearing bands and quartz and plagioclasio-bearing bands. C) Intermediate halo: light gray, foliated rock composed of carbonaceous matter, quartz, and carbonates with sulfide-rich domains. D) Proximal Halo: light gray rock composed of quartz, carbonate, carbonaceous material, and sulfides. The foliation is partially obliterated by quartz veins and silicification. (E and F) Photomicrographs of the carbonaceous schist of the Crixás greenstone belt. The rock has domains composed of carbonaceous material and biotite alternated with granoblastic domains of fine-grained quartz, plagioclase, and garnet. Abbreviations: Bt – biotite; Grt – garnet; Pl – plagioclase; Qtz – quartz.

or carbonate-rich veins are common in this unit.

Carbonaceous schists consists mainly of quartz (ca. 20–40 vol%), carbonaceous matter (ca. 60–50 vol%), and biotite (ca. 3–20 vol%), as well plagioclase (ca. 3–10 vol%), muscovite (ca. 0–10 vol%), chlorite (ca. 1–10 vol%) and garnet (ca. 1–8 vol%) in smaller proportions. Pyrrhotite, chalcopyrite, arsenopyrite, ilmenite, and zircon are common minerals and constitute <1% of the mineral assemblage. Lepidoblastic texture domains are defined by the orientation of biotite, chlorite, and muscovite dispersed among the carbonaceous matter that commonly exhibits folding and crenulation. Anhedral quartz and plagioclase with oligoclase to andesine compositions (Appendices B and C) constitute fine-grained, recrystallized domains (Fig. 7e and f). Garnet occurs as subhedral crystals ranging from 0.05 to 0.2 mm or as porphyroblasts up to 0.7 mm with inclusions of the groundmass minerals.

4.1.2.2. Distal hydrothermal alteration halo. The effects of the hydrothermal alteration process on the distal halo are slightly pervasive, resulting in few mineralogical and textural modifications compared to the intermediate and proximal halos. The dark grayish rock is characterized by alternating millimeter carbonaceous matter and micaceous mineral-bearing layers with the quartz-rich layers (Fig. 7b). The tectonic foliation is characterized by a spaced schistosity, with a preferential mica and chlorite orientation.

The rock mineral composition consists of quartz (ca. 40 vol%), biotite (ca. 30 vol%), chlorite (ca. 20–25 vol%), carbonaceous material (ca. 20–25 vol%), muscovite (ca. 20 vol%), plagioclase (ca. 5 vol%), and garnet (ca. 2 vol%). Ilmenite, pyrrhotite, and chalcopyrite comprise <1 vol% of the modal composition. The texture is defined by lepidoblastic domains, marked by the orientation of biotite and chlorite lamellae according to the rock foliation, alternated with granoblastic domains defined by fine-grained recrystallized quartz and plagioclase. Anhedral garnet porphyroblasts are common and may exhibit poikiloblastic texture, with inclusions of the matrix minerals. Garnet also occurs as fine to medium-grained crystals. Chlorite occurs oriented, replacing biotite.

The distal halo is characterized by a slight increase in chlorite and white mica, and a decrease in carbonaceous material. Mineral chemistry data indicate that the white mica corresponds to muscovite. Plagioclase is classified as oligoclase (Appendices B and C).

4.1.2.3. Intermediate hydrothermal alteration halo. The intermediate halo is characterized by a fine-grained grayish rock, composed of carbonaceous matter and micaceous minerals. Sulfide-rich and colorless domains, composed of quartz and carbonate, are also observed. Quartz and carbonate veinlets are common (Fig. 7c).

The mineral assemblage consists of quartz (ca. 35–45 vol%), muscovite (ca. 25–39 vol%), carbonate (ca. 12–15 vol%), carbonaceous matter (ca. 10–15 vol%), biotite (ca. 3–6 vol%), and chlorite (ca. 3 vol %). Allanite, apatite, rutile, tourmaline, pyrrhotite, arsenopyrite, chalcopyrite, and ilmenite occur as accessory minerals, comprising <1 vol% of the modal composition. The rock is characterized by lepidoblastic texture domains with biotite, chlorite, and muscovite lamellae oriented according to the tectonic foliation. Granoblastic domains composed of medium to coarse-grained quartz and carbonate crystals also occur (Fig. 8a and b). Quartz is present as anhedral crystals, with irregular contacts and undulating extinction. Sulfides occur as fine to medium-grained anhedral crystals, represented by pyrrhotite and arsenopyrite. Chalcopyrite is rare and always associated with pyrrhotite crystals. Very fine-grained tourmaline occurs as clusters of tabular crystals with light

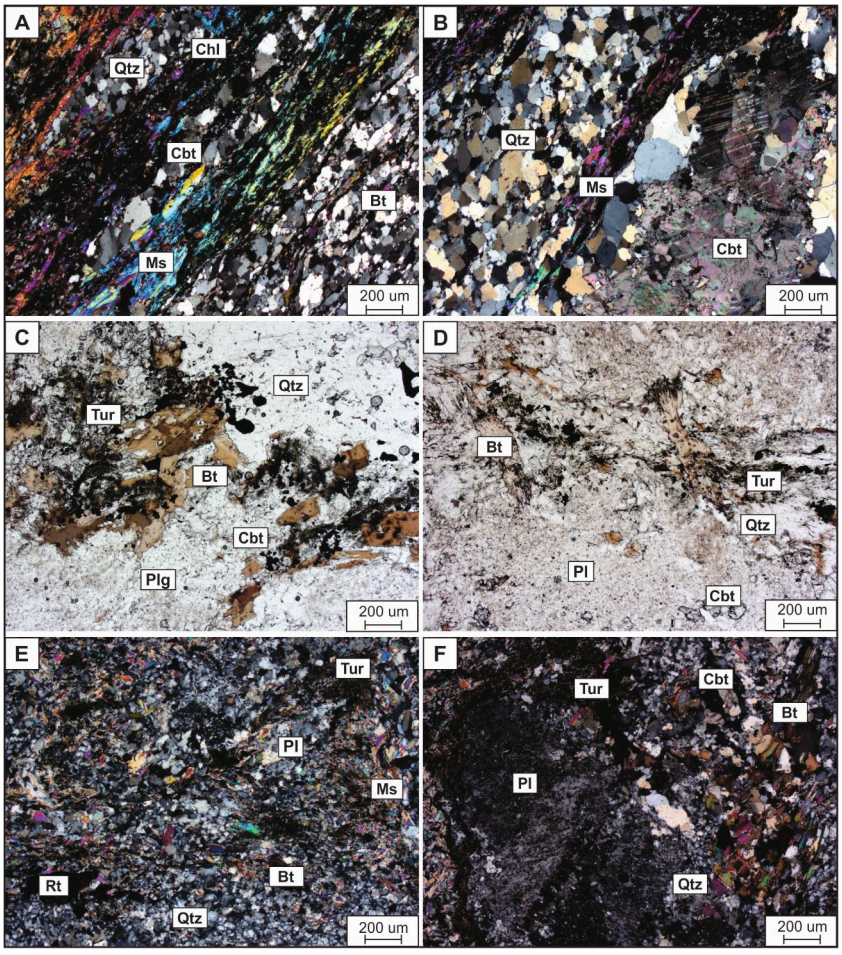

Fig. 8. Photomicrographs of Structure IV hydrothermal alteration halos. A and B) Intermediate Halo: lepidoblastic domains with muscovite, biotite, chlorite, and carbonaceous matter-bearing layers alternated with granoblastic recrystallized quartz and carbonate domains. C and D) Proximal halo: biotite porphyroblasts and tourmaline clusters, and quartz, carbonate, and plagioclase layers. E) Proximal halo: fine-grained and recrystallized granoblastic matrix composed of quartz, plagioclase, carbonate, and rutile, with biotite and muscovite lamellae. F) Proximal halo: coarse-grained plagioclase surrounded by tourmaline cluster and biotite lamellae in a recrystallized matrix composed of quartz, plagioclase, and carbonate. Abbreviations: Bt – biotite; Cbt – carbonate; Chl – chlorite; Ms – muscovite; Pl – plagioclase; Qtz – quartz; Rt – rutile; Tur – tourmaline.

greenish pleochroism.

Chlorite compositions correspond to ripidolite and plagioclase is classified as oligoclase. Carbonate is classified as Fe dolomite (Appendices B and C).

In this halo, the hydrothermal process is more evident due to quartz, carbonate, and muscovite enrichment, accompanied by decreasing biotite, carbonaceous matter, and chlorite.

4.1.2.4. Proximal hydrothermal alteration halo. The proximal halo is characterized by a massive light-gray rock composed predominantly of quartz and carbonate, with some domains consisting of relics of lamellar minerals and carbonaceous matter. Sulfide-rich domains are recurrent (Fig. 7d).

The proximal halo consists mainly of quartz (ca. 40–45 vol%), plagioclase (ca. 20–30 vol%), carbonate (ca. 15–20 vol%), carbonaceous matter (ca. 5–10 vol%), biotite (ca. 5–10 vol%), muscovite (ca. 3–8 vol %), and tourmaline (ca. 2 vol%). Chlorite, rutile, allanite, and apatite constitute <1 vol% of the modal composition. Sulfides are represented by arsenopyrite, pyrrhotite, and chalcopyrite and may constitute <5 vol % of the mineral assemblage. Arsenopyrite is the predominant sulfide phase, and chalcopyrite occurs eventually as very fine-grained crystals. The predominant rock texture is granoblastic, characterized by medium-grained recrystallized aggregates of quartz, carbonate, and plagioclase. Locally, idioblastic and lepidoblastic domains occur with oriented muscovite and biotite lamellae. Biotite may be replaced by chlorite (Fig. 8e).

Muscovite appears as very thin lamellae. Biotite occurs as fine-grained lamellae dispersed in the rock matrix and as porphyroblasts up to 1.5 mm. Tourmaline is present as very fine-grained tabular crystals with greenish pleochroism occurring mainly concentrated in irregular domains and surrounding plagioclase and biotite porphyroblasts (Fig. 8c and d). Plagioclase is commonly saussuritized and occurs as fine-grained anhedral crystals or as coarse grains with inclusions (Fig. 8e and f).

The mineral assemblage and textures suggest an intense hydrothermal alteration zone where the original mineralogy was completely altered, and the foliation was obliterated.

Mineral chemistry data (Appendices B and C) indicate oligoclase composition for the plagioclase in this halo. Chlorite is classified as ripidolite, similar to the other halos. White mica composition corresponds to muscovite, and carbonate is Fe dolomite.

4.2. Reflectance spectroscopy

Reflectance spectroscopy allowed identifying different mineral groups, such as: chlorite (Mg chlorite, Mg-Fe/Fe-Mg chlorite, and Fe chlorite), hornblende, carbonate (ankerite, calcite, and dolomite), white mica (muscovite and paragonite), epidote and talc (Fig. 9).

4.2.1. Chlorite

The chlorite spectrum is characterized by two main SWIR absorption features; one between 2240 and 2270 nm, related to the Fe-OH bond or Al(Mg, Fe)–OH (Lypaczewski and Rivard, 2018), and another between 2317 and 2365 nm associated with Mg-OH (Clark et al., 1990; King and Clark, 1989). The positions of both absorption features change according to the chlorite composition, shorter and longer wavelengths indicate Mg-rich and Fe-rich compositions, respectively (McLeod et al., 1987). Mg chlorite exhibits absorption features at approximately 2240–2255 nm and 2319–2342 nm (Yang et al., 2005). Absorption features at 2250–2262 nm and 2342–2365 nm characterize intermediate Mg-Fe chlorites whereas 2257–2265 nm and 2355–2365 nm characterize Fe chlorites (Fig. 9; Yang et al., 2005).

In the present study, the drill core samples show that chlorite is the

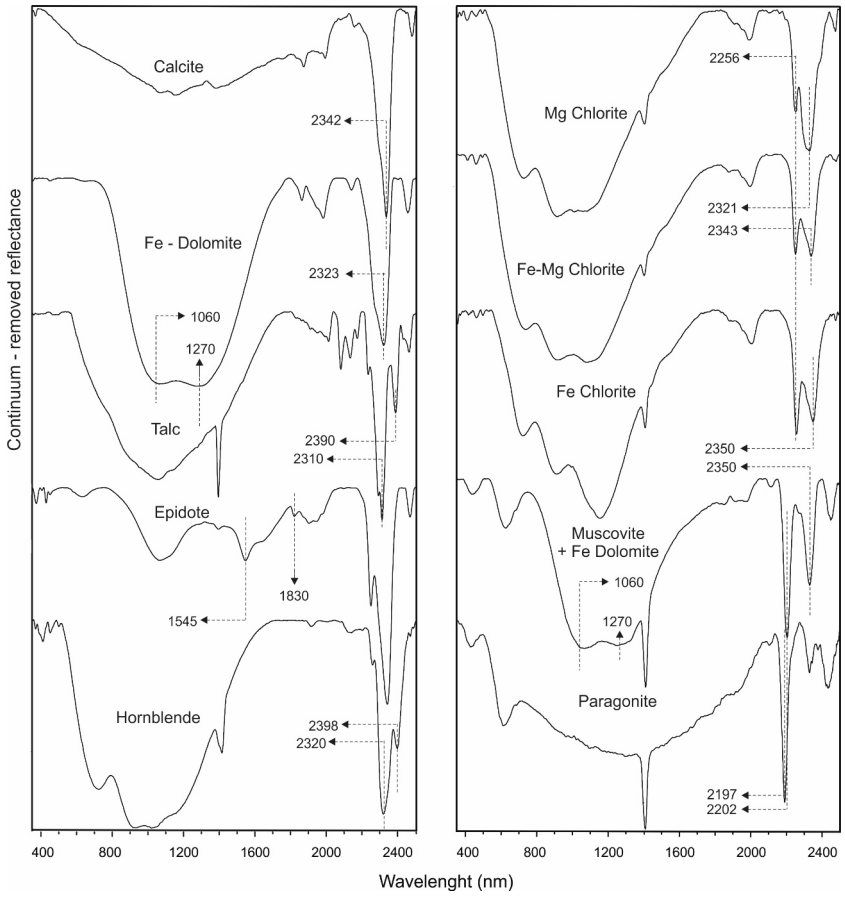

Fig. 9. Stacked continuum-removed reflectance spectra of minerals identified in the rock samples from the CPIVESD0031 drill hole.

most abundant mineral. The parameter 2340Dcl (Appendix A) uses the depth of the ~2340 nm absorption feature to calculate chlorite relative abundance. Chlorite was identified in spectra commonly associated with carbonate (calcite, Fe-dolomite and ankerite) and epidote. In the CPIVEDS0031 drill core samples, chlorite occurs predominantly in the hydrothermalized mafic rock represented by quartz-chlorite-carbonate-sericite schist and chlorite-garnet schist, including in the hydrothermal alteration halos of the Palmeiras Structure, and occasionally in the metabasalt. In the carbonaceous schist unit, chlorite content is lower and related to hydrothermalized zones as well (Fig. 10).

Chlorite composition (2340Wvl, Appendix A) was defined by the position of the ~2340 nm absorption feature. The results were plotted in a frequency histogram to identify the compositional variation that shows the predominance of Mg-rich and Fe/Mg-rich chlorite compositions, and less Fe-rich chlorite. The most Fe-enriched chlorite occurs predominantly in the hydrothermal zones of the Palmeiras Structure and Structure IV, whereas Mg-enriched chlorite occurs in unaltered host rock (Fig. 10). This result was confirmed by the mineral chemistry analysis (Appendix C).

4.2.2. *Hornblende*

Hornblende is characterized by Mg-OH-related diagnostic features between 2300 and 2330 nm, and between 2375 and 2400 nm (Fig. 9; Hunt, 1977). In this study, the parameter 2320Danf was used to define hornblende relative abundance considering the depth of ~2320 absorption-feature (Appendix A). Along the drill hole, hornblende is the second most abundant mineral and is predominantly associated with the metabasalt unit, also occurring in some hydrothermalized metabasalt domains, such as quartz-chlorite-carbonate-sericite schists (Fig. 10).

4.2.3. *Carbonates*

The spectral signature of carbonates is characterized by CO_3^{2-} related absorption features in, 2300–2350 nm and three other minor features in 1870–1886 nm, 1985–2008 nm and 2135–2170 nm (Gaffey, 1986). The absorption feature at ~2300 nm occurs as a function of the carbonate composition and can vary between 2306 and 2330 nm (dolomite), 2316–2340 nm (ankerite), and 2327–2349 nm (calcite).

The carbonate abundance algorithm 2328Dc (Modified from Prado et al., 2016; Appendices A) considered the depth of the absorption feature at ~2328 nm. The results indicate that carbonate predominates in the dolomite layers, but it also occurs in zones of hydrothermalized metabasalts and carbonaceous schists.

The carbonate composition parameter (2328 Wvl, Appendix A) considers the wavelength position of the ~2328 nm absorption feature for distinguishing calcite, dolomite and ankerite. The results indicate the predominance of dolomite in the drill hole samples (Fig. 11). Ankerite and Fe-dolomite occur strictly in mineralized structures (Fig. 10). Calcite occurs in quartz-carbonate veinlets hosted in volcanic mafic rocks (Fig. 10). Even though iron carbonates may also be identified by the Fe^{2+} absorptions features in ~1060 and ~1270 nm (Fig. 9; Hunt and Salisbury, 1971; Gaffey, 1986; Clark et al., 1990; Clark, 1999), in this study these absorptions features were not efficient for calculating the carbonate parameters.

4.2.4 White mica

The Al-OH related absorption feature near 2200 nm is a function of the Al content in the octahedral cation sites and defines the white mica spectrum signature (Vedder and McDonald, 1963; Post and Noble, 1993). Absorptions between 2180 and 2190 nm correspond to paragonite (Na-rich white mica), while features between 2200 and 2208 nm characterize Al-rich muscovite (Fig. 11). Al-poor phengite is identified by absorptions between 2216 and 2228 nm (Post and Nobe, 1993).

In this study, the white mica relative abundance was defined by the parameter 2200Dwm, which is calculated by the depth of ~2200 nm absorption feature (Appendix A). The results exhibit the presence of white micas in the hydrothermalized mafic rock domains, dolomites, and carbonaceous schist, including the hydrothermal alteration halos of the Palmeiras Structure and Structure IV.

The parameter 2200Wvl determines the white mica composition as a

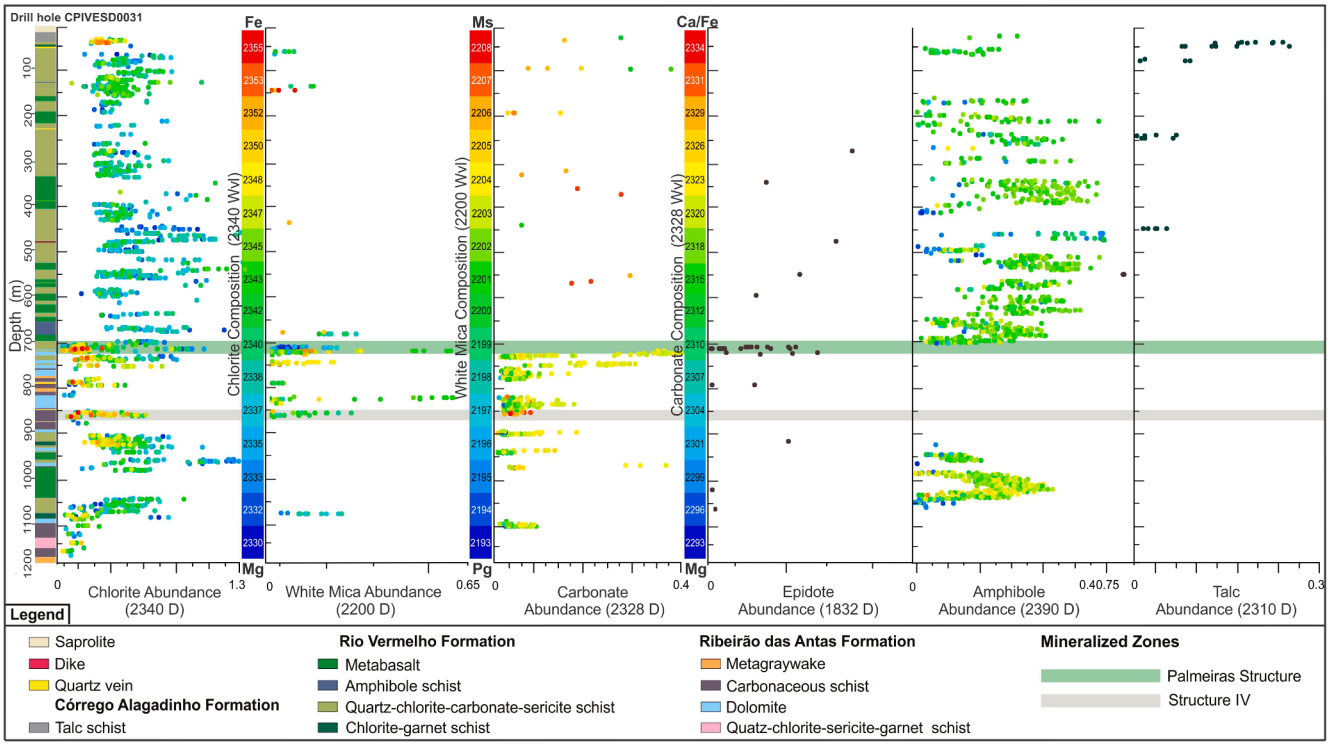

Fig. 10. Results of the composition and relative abundance spectral parameters calculations in relation to the different lithological units and mineralized zones along the CPIVESD0031 drill hole.

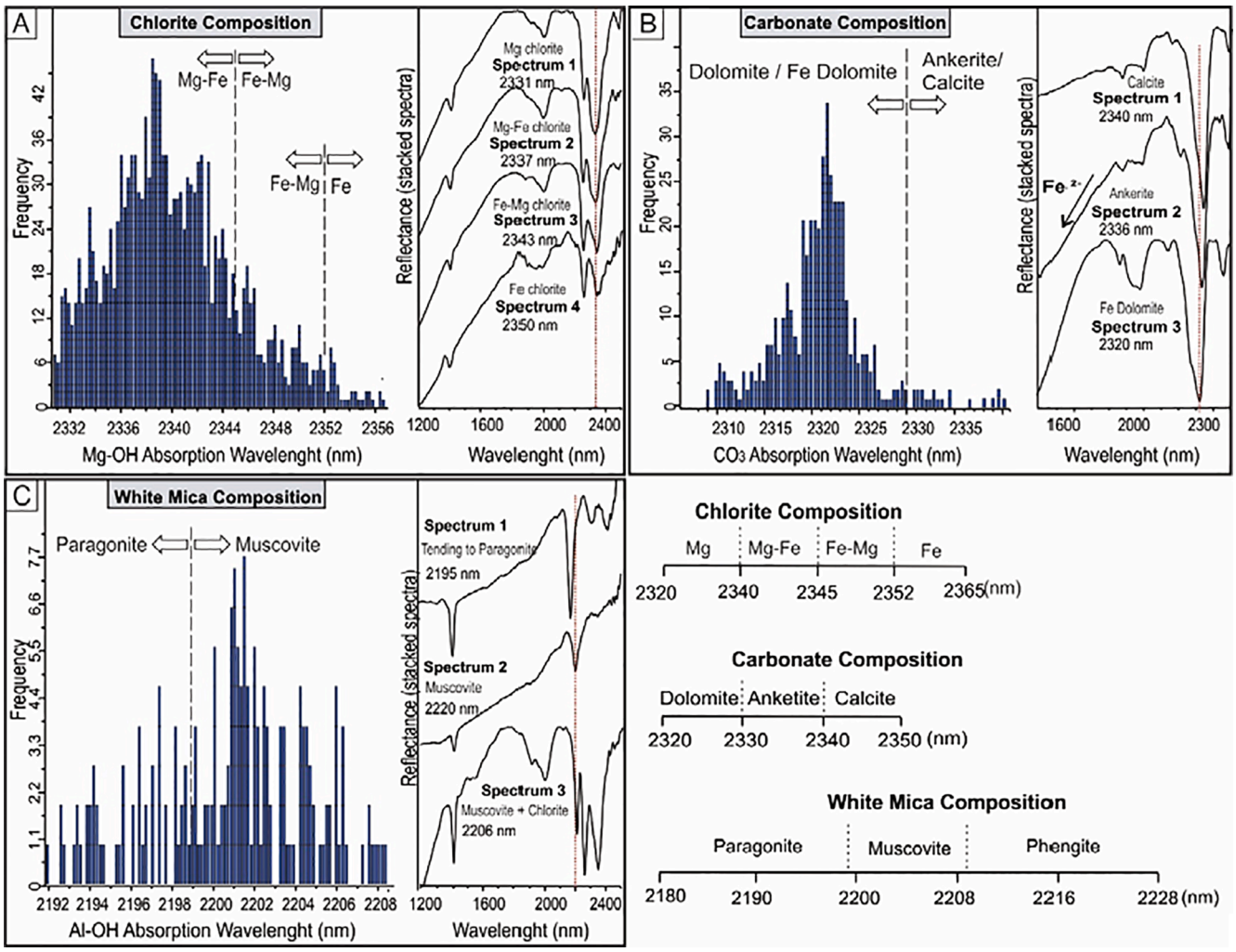

Fig. 11. Histogram showing the varying composition of chlorite, carbonate and white mica based on spectral data. The representative SWIR spectra of each identified mineral composition are displayed to the right of each histogram.

function of the absorption feature position observed near the 2200 nm wavelength. The results were plotted in the histogram (Fig. 11), where it is observed white mica compositions tending to paragonite with absorptions ranging between 2192 and 2200 nm that occurs strictly in the Palmeiras Structure proximal halo (Fig. 10). Also, muscovite spectra with absorption features between 2200 and 2209 nm (Fig. 11) are observed and it occurs preferably in the alteration halos of the Palmeiras Structure and Structure IV (Fig. 10).

4.2.5. Epidote

Epidote was identified in spectra based on the OH absorption features at ~1550 and ~1830 nm (Yang et al., 2005) since its most prominent Fe-OH-related absorptions at ~2255 and ~2340 nm (Liebscher, 2004) overlap the diagnostic features of chlorite and carbonates in mineral mixtures The 1550D relative abundance parameter was defined based on the depth of the ~1550 nm feature. The result showed that epidote occurs predominantly in the Palmeiras Structure hydrothermal zone, with some occasional occurrences in the non-hydrothermalized metabasalt (Fig. 10).

4.2.6 Talc

Talc can be identified by the doublet MgOH- related feature at ~2288 and ~2310 nm, and by the secondary feature at ~2387 nm (Fig. 9; Clark et al., 1990). The 2290D algorithm was used to define the relative abundance of talc in drill core samples, based on the analysis of the depth of the absorption feature at ~2387 nm (Appendix A). The results indicated that talc occurs strictly in the talc schist at the top of the CPIVESD0031 drill hole and in some samples of quartz-chlorite-carbonate-sericite schist (Fig. 10).

4.3. Geochemistry of mineralized zones

4.3.1. Palmeiras Structure

The major element analyses indicate a significant K_2O, BaO and LOI increase in the hydrothermalized metabasalt, and even higher in the three alteration halos associated with the Palmeiras Structure (Fig. 12). Also, progressive Na_2O, Fe_2O_3, Ti_2O, Al_2O_3, and Cr_2O_3 enrichment is observed toward the proximal halo (Fig. 12). The distinct behavior of MnO showed increasing concentrations in the distal and intermediate halos, followed by significant depletion in the proximal halo. And CaO, MgO, and P_2O exhibited progressive depletion toward the proximal halo (Fig. 12).

Analyses of trace elements show that hydrothermal alteration halos have significant enrichment in Ba, Cs, Rb, U, Li, W, and ETR (Fig. 12). Whereas V, Co, Cd, and Zn concentrations increased less along the hydrothermal alteration zone (Fig. 12).

4.3.2. Structure IV

Despite the chemical differences observed between the hydrothermal

Fig. 12. A) Results of the ratio calculations between the concentration of the chemical elements in the hydrothermal halos and unaltered host rocks along the Palmeiras Structure. Ratios below 1 indicate element depletion, whereas ratios above 1 indicate element enrichment. B) Chemical behavior of selected elements in the metabasalt and quartz-chlorite-sericite schist samples, as well as in the hydrothermal halos along the Palmeiras Structure.

alteration halos and the host metasedimentary rocks (Fig. 13), the geochemical changes were less pronounced in the hydrothermal alteration halos of Structure IV compared to the Palmeiras Structure.

The results on major elements indicate SiO_2 and CaO enrichment in all hydrothermal alteration halos. Also, Na_2O and P_2O increased in distal and proximal halos and decreased the intermediate halo. K_2O increased in the intermediate halo, with lower concentrations in the distal and proximal halos (Fig. 13). On the other hand, Fe_2O_3, MgO, and MnO show progressive depletion towards the proximal halo (Fig. 13). Al_2O_3 and TiO_2 also display a decrease in their concentrations in all the hydrothermal halos (Fig. 13).

Regarding trace elements, As, Sb, W, Te, and Re exhibit higher concentrations in the hydrothermal alteration halos than the host rock. Mo, Bi, and S, also increase in the proximal halo (Fig. 13).

4.4. Physical properties of rocks

Table 1 presents the statistical analyses (mean, minimum and maximum values) and the measured physical properties, density and magnetic susceptibility, of the lithological components of the rock samples collected in the CPIVESD0031 drill hole.

4.4.1. Density

The density values vary between 3.880 and 2.130 g/cm^3 (Table 1; Fig. 14). The ultramafic unit is represented by talc schist with an average density close to 2,884 g/cm^3 and a small range between 2.812 and 2.956 g/cm^3 (Fig. 14).

Metabasalt and amphibole schist average densities are close to 3.009 g/cm^3 and 3.080 g/cm^3, respectively, ranging from 2.786 to 3.67 g/cm^3 for metabasalt and from 2.875 to 3.2 g/cm^3 for amphibole schist (Table 1). Anomalous values such as densities below the average determined for metabasalt indicate hydrothermalized samples or samples with amygdala and venulations (Fig. 14). The density of hydrothermalized metabasalts, such as quartz-chlorite-carbonate-sericite schist and chlorite-garnet schists, decreases significantly due to the replacement of metamorphic minerals with less dense hydrothermal alteration minerals.

The average density of quartz-chlorite-carbonate-sericite schist is 2.876 g/cm^3, ranging from 2.5 to 3.576 g/cm^3 (Table 1). Anomalous values such as higher-than-expected densities correspond to samples from the Palmeiras Structure proximal halo (highlighted in Fig. 14). This density increase is a response to Fe enrichment as indicated by the magnetite abundance in the mineral assemblage as well as the mineral chemistry data of chlorite and carbonate.

The average density of chlorite-garnet schist is close to 2.879/cm^3 with a relatively broad range, between 2.428 and 3.727 g/cm^3 (Table 1), whereas anomalous density values between 3.33 and 3.47 g/cm^3 were obtained for the domain below the Palmeiras Structure.

The dolomite density values range from 2.130 to 3.733 g/cm^3, with an average of 2.825 g/cm^3 (Table 1). The outliers in Fig. 14 correspond to the dolomite layer below the Palmeiras Structure, which occurs in contact with chlorite-garnet schist.

The carbonaceous schist has the lowest average density of 2.781 g/cm^3, ranging from 2.471 to 3.880 g/cm^3 (Table 1). Although hosted in this unit, the density values of the Structure IV samples have no significant changes (Fig. 14). Carbonaceous schist samples with higher densities also occur, indicating high contents of sulfides and garnet, commonly in contact with the quartz-chlorite-sericite-garnet schist levels (Fig. 14).

On the other hand, quartz-chlorite-garnet-sericite schist has the highest average density of 3.03 g/cm^3, ranging from 2.933 to 3.165 g/cm^3 (Table 1). Compared to the other rocks, this high density is due to the abundance of minerals such as garnet and amphibole in the mineral assemblage. Quartz-chlorite-sericite schist represents a hydrothermalized metagraywacke level. Metagraywacke has a lower average density of 2.802 g/cm^3, ranging from 2.658 to 2.980 g/cm^3 (Table 1).

4.4.2. Magnetic susceptibility

The magnetic susceptibility values of the drill core samples ranged from 0.006 to 1424.545×10^{-3} SI (Table 1; Fig. 14). Magnetic susceptibility is lower in metasedimentary compared to the mafic and ultramafic metavolcanic rocks. The lowest average magnetic susceptibility value of 0.120×10^{-3} SI was obtained for dolomite, followed by 0.385×10^{-3} SI for metagraywacke, and 0.421×10^{-3} SI for carbonaceous schist (Table 1).

Talc shale is the lithological unit with the highest mean MS value of 4.491×10^{-3} SI. However, the highest MS values recorded (up to $1424{,}545\times10^{-3}$ SI) are related to the presence of magnetite in the hydrothermal alteration halos of the Palmeiras Structure, highlighted in red in Fig. 14. The garnet shale domain in contact with the Palmeiras Structure also has outliers that can reach up to $75{,}632\times10^{-3}$ SI.

5. Data integration and discussion

5.1. Palmeiras Structure

The Palmeiras Structure is a low-angle thrust fault that occurs parallel and next to the contact with the metasedimentary unit (Fig. 2c) and intercepts the hydrothermal metabasalt, displaying intense hydrothermal alteration (Massucato, 2004; Almeida and Aurífera, 2006), which is approximately 10 m wide at 750 m deep in the CPIVESD0031 drill hole. According to unpublished data by AngloGold Ashanti, the gold grade can be up to 31 g/t.

The metamorphic paragenesis of the metabasalt, represented by hornblende + oligoclase, indicates the lower amphibolite facies metamorphic conditions. Hydrated mineral phases, stable at lower temperatures, completely replaced the metamorphic assemblage as a result of the hydrothermal processes. Fig. 4 shows the paragenetic sequences established for each hydrothermal halo of the Palmeiras Structure.

The distal halo is dominated by chloritization, biotitization, and incipient carbonation. The mineral assemblage is represented by Fe-Mg chlorite + biotite + ankerite + quartz ± epidote ± hornblende ± ilmenite ± oligoclase (Fig. 4). Hornblende occurs as a relic of the peak metamorphic assemblage.

The intermediate hydrothermal alteration is defined by epidotization and carbonation. The resulting halo is characterized by a mineral assemblage of epidote + ankerite + Fe-Mg chlorite + biotite + quartz ± ilmenite ± magnetite ± muscovite ± oligoclase (Fig. 4). This halo is defined by the complete absence of hornblende as well as the formation of epidote and carbonate porphyroblasts.

The proximal halo is dominated by muscovite-rich alteration and the mineral assemblage consists of muscovite + Fe-Mg chlorite + magnetite + quartz ± ilmenite ± oligoclase ± paragonite ± tourmaline. Biotite has been entirely replaced by chlorite whereas ankerite and epidote occur as minor components (Fig. 4).

The sulfide phase, composed of pyrite and chalcopyrite, occurs throughout the Palmeiras Structure and its amount does not increase when compared to the unaltered host rock. Therefore, this mineral phase cannot be considered as diagnostic for hydrothermal alteration halos.

Mineral chemistry results indicate that the hydrothermal processes did not modify plagioclase since the same oligoclase composition is observed in both non-altered metabasalt and hydrothermal alteration halos. However, chlorite and carbonate exhibit progressive Fe enrichment towards the proximal zone of the Palmeiras Structure; this Fe enrichment is also observed in the geochemical data (Fig. 15).

The reflectance spectroscopy was useful to recognizing the Palmeiras Structure since it allowed identifying the chlorite, white mica, and epidote relative abundance, besides assessing their compositional variation (Fig. 15). Although petrographical data indicated carbonate-rich zones in Palmeiras Structure, they were not fully identified by reflectance spectroscopy. The Palmeiras Structure samples are composed of several minerals with FeOH and MgOH related absorptions features (chlorite, biotite, epidote and amphibole) that, in spectral mixtures, can

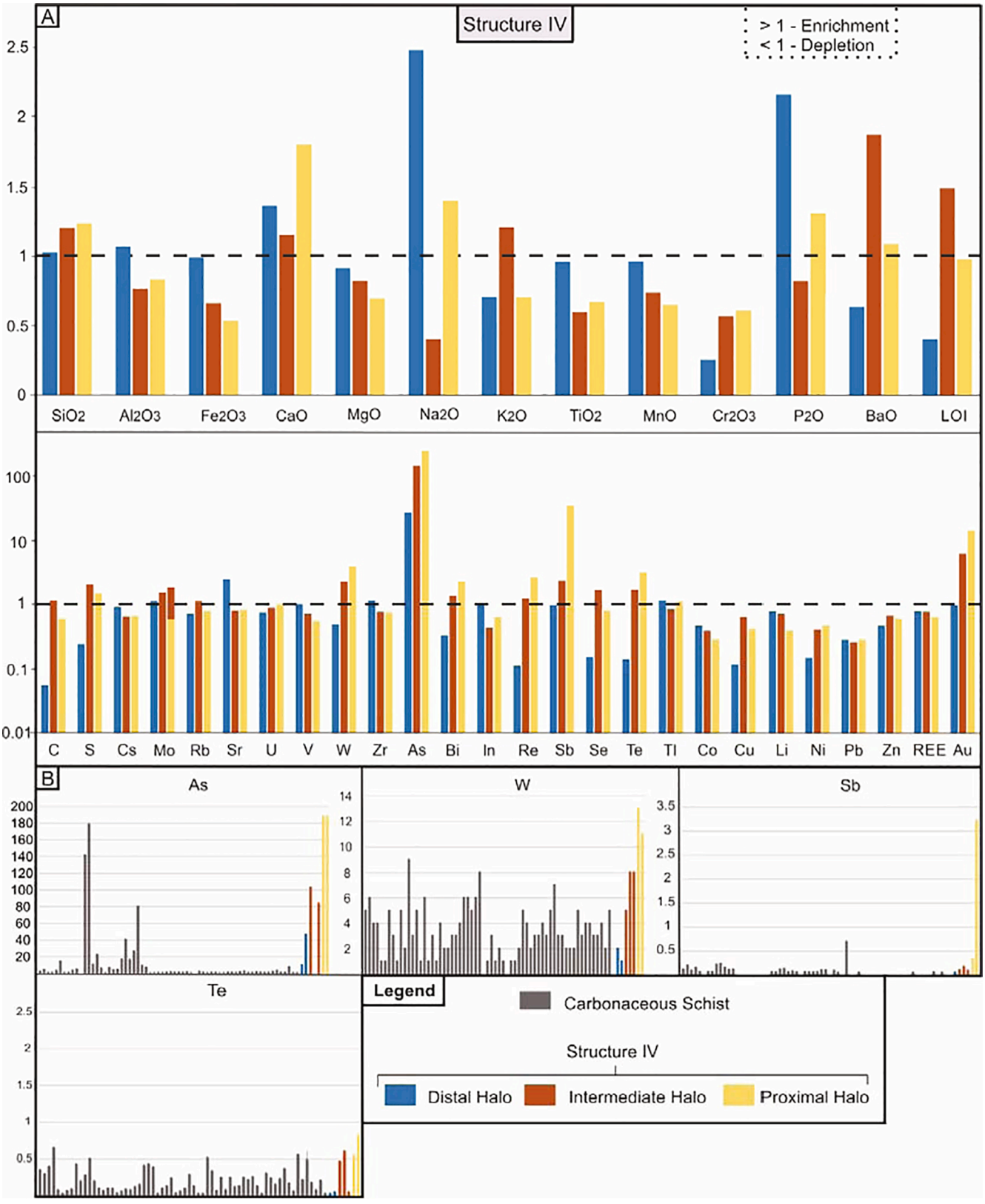

Fig. 13. A) Results of the ratio calculations between the concentration of the chemical elements in the hydrothermal halos and unaltered host rocks along the Structure IV. Ratios below 1 indicate element depletion, whereas ratios above 1 indicate element enrichment. B) Chemical behavior of selected elements in the carbonaceous schist samples and in the hydrothermal halos along the Structure IV.

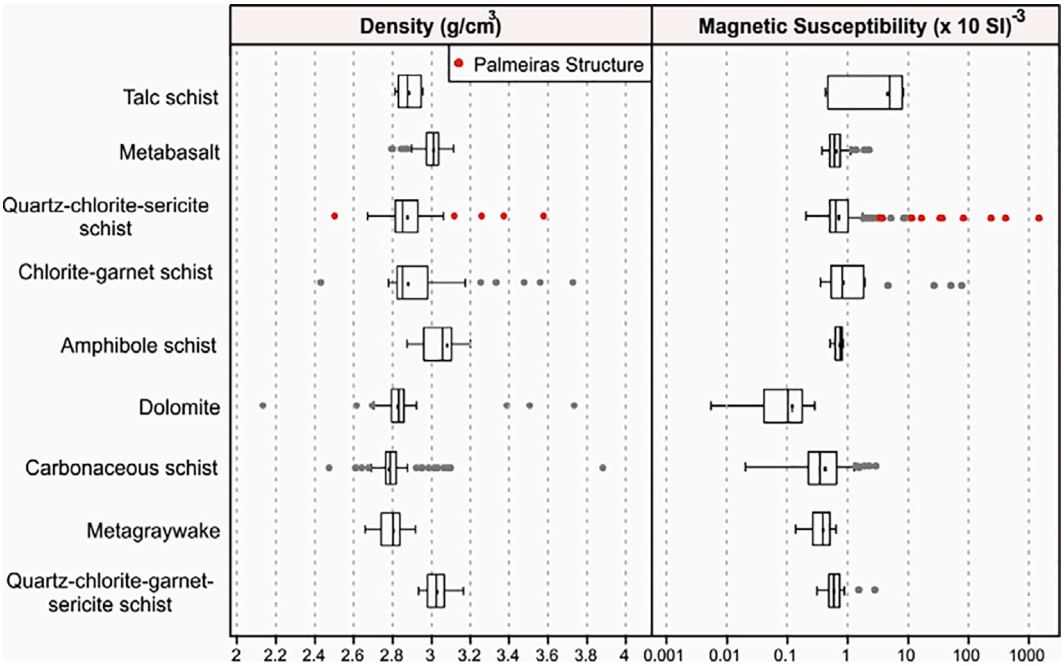

Fig. 14. Box plots showing the ranges, averages, and outliers values of the density and magnetic susceptibility measured in each drill hole lithology. The anomalous values of physical properties associated with mineralized structures are highlighted in red. (For interpretation of the references to colour in this figure legend, the reader is referred to the web version of this article.)

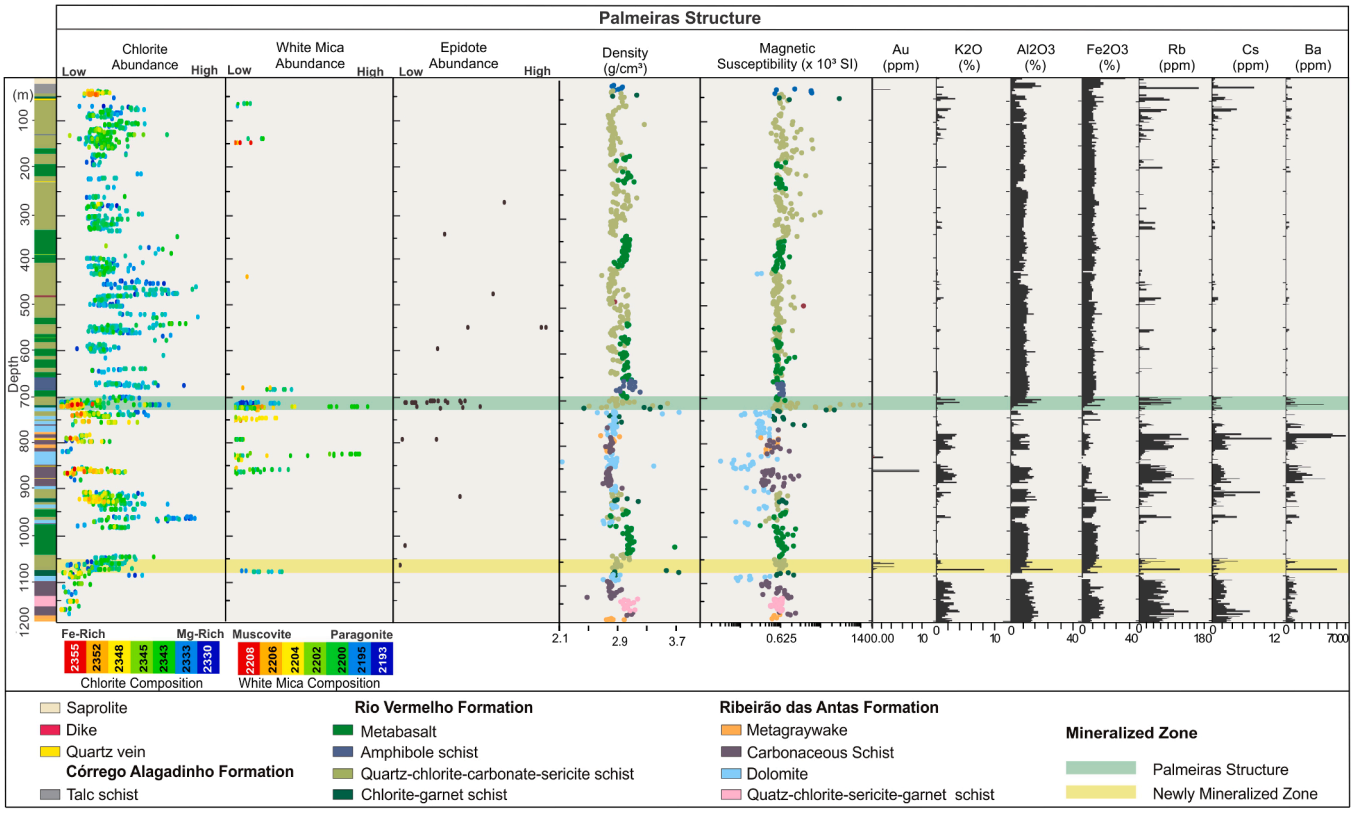

Fig. 15. Synthesis of the spectral, geochemical, and petrophysical signature of the hydrothermal alteration halos of the Palmeiras Structure.

share the wavelength position of the main carbonate absorption features. If the carbonate content is low concerning the chlorite content in a spectral mixture, its diagnostic absorption feature will overlap in ~2340 nm, becoming more difficult to calculate the carbonate relative abundance.

The geochemical results highlighted a progressive increase in the concentration of alkalis (K_2O, Na_2O, Rb, Cs, Li, and Ba) towards the mineralized zone (Fig. 15). Such enrichment was identified throughout the hydrothermalized metavolcanic rocks. Previous studies have shown that the increased alkali concentrations in gold mineralizations hosted in

mafic rocks constitute much larger geochemical halos than visible hydrothermal alteration halos (Heath and Campbell, 2004). The study on the mobility of these elements can, therefore, be used as a promising tool in gold prospecting since the alkali distribution may indicate the path of fluid percolation (Gaillard et al., 2020). Increased alkali concentrations near the mineralization levels may define an important vector toward gold mineralization exploration (Xu, 1999; Heath and Campbell, 2004; Bacha et al., 2021).

The increase of alkalis in the hydrothermalized mafic rocks occurs due to feldspar breakage and loss of potassium and LILEs such as Cs and Rb (Heath and Campbell 2004), which in turn enrich micas, clays, and other secondary minerals as the hydrothermal fluids migrate to more distal portions of the mineralized zones. Cs and Rb commonly replace K in hydrated minerals such as micas, for example, causing the LILEs to fractionate between the hydrothermal fluid and host rock so these elements can be more useful indicators of fluid percolation than K (Melzer and Wunder, 1999). This suggests that the increased alkali in the Palmeiras Structure alteration halos may also be related to feldspar breakage and subsequent incorporation of alkalis in the identified hydrated mineral structures.

The chemical behavior of elements also indicates a progressive increase in Al_2O_3, Fe_2O_3, Cr_2O, and TiO_2 concentrations in the intermediate and proximal halos, associated with the progressive stabilization of chlorite, muscovite, and magnetite. The gain of Na_2O in the proximal halo can be related to paragonite formation. Less significant U, W, Th, Ta, Hf, Nb, and Zr concentrations were also evidenced in the proximal halo.

Because no thermo-barometric studies have been performed on the Palmeiras Structure minerals, the hydrothermal fluid physicochemical conditions cannot be defined. On the other hand, the geochemical and petrographic data indicated the addition of alkalis and iron, as well as CO_2 due to the carbonation zones.

Petrophysical anomalies assist in characterizing ore deposits hosted in greenstone belts. The orebody magnetization depends on the concentration of magnetic minerals in the rock, which can be generated or destroyed by the hydrothermal/metamorphic processes associated with mineralization. Also, the content, shape, and size of ferromagnetic mineral grains and Fe concentration in the rock affect the magnetic susceptibility directly (Gunn and Dentith, 1997; Airoing and Mertanen, 2008; Airo, 2015; Dentith and Mudge, 2014; Dentith et al., 2020).

Anomalous values of magnetic susceptibility data were observed, with values ranging from 0.425 to 1425.00×10^{-3} SI (Table 1; Fig. 14) and individual values varying significantly from one sample to another. These significant differences are probably explained by the different content, size, and shape of ferromagnetic, paramagnetic, and diamagnetic minerals, as well as higher Fe concentrations.

Individual analysis of the alteration halos shows average magnetic susceptibility values of 1.187×10^{-3} SI, 10.457×10^{-3} SI, and 305.96×10^{-3} SI for the distal, intermediate, and proximal halos, respectively. Thus, it is observed that the average magnetic susceptibility values increase progressively as the magnetite concentration increases in the direction of the proximal halo of the Palmeiras Structure.

The Palmeiras Structure density data also exhibit anomalous average values for the samples from the CPIVESD0031 drill hole (Fig. 15). The average density values of 2.808, 2.967, and 3.068 g/cm^3 were calculated for distal, intermediate, and proximal halos, respectively. Similar to the magnetic susceptibility values, the average densities increased linearly towards the internal zone of the Palmeiras Structure. A direct correlation between high values of magnetic susceptibility and density with increasing Fe concentration can be observed in the samples, allowing us to conclude that density increase is a direct response to the presence of magnetite.

In summary, the hydrothermal footprint of the Palmeiras Structure is composed of a distal halo marked by chloritization, biotitization, and ± carbonation, an intermediate halo defined by the epidotization, carbonation ± chloritization, and a proximal halo marked by sericitization ± chloritization.

Reflectance spectroscopy highlighted the rocks with Fe- enriched chlorite, white mica (muscovite and paragonite), and epidote, suggesting that these minerals can be used as guides towards the orebodies along the Palmeiras Structure. The geochemical signature is characterized by the significant increase in K_2O, Rb, Cs, Li, and Ba concentrations, as well as smaller gains in Na_2O, Fe_2O_3, Al_2O_3, TiO_2, LOI, U, W, Th, Ta, and ETR. The physical properties exhibit significant magnetic susceptibility anomalies related to the magnetite present in the proximal halo, accompanied by rock density increase (Fig. 15).

Fig. 15 shows the main parameters of the Palmeiras Structure hydrothermal footprint. Note that the exploratory vectors defined for the Palmeiras Structure highlighted another unknown mineralized zone, which is also hosted in the hydrothermalized metabasalts nearly 1060 m deep with gold grade up to 4.3 g/t and stands out for the presence of chlorite and white mica, as well as K_2O, Rb, Cs, Li, and Ba enrichment, similar to the Palmeiras Structure. The absence of magnetite explains the lack of anomalous values of density and magnetic susceptibility. Enrichment in the pathfinder elements As, W, Sb, and Re was observed as well (Fig. 16).

5.2. Structure IV

Structure IV is defined as a high-strain deformation zone that intercepts the carbonaceous schists, in which the mineralization is either related to disseminated ore or quartz veins. Previous studies (Petersen, 2003; Sobiesiak, 2011; Souza, 2018) on several orebodies controlled by Structure IV determined that the ore occurs associated with intense silicification zones, accompanied by quartz and sulfide veinlets with arsenopyrite, pyrrhotite, and chalcopyrite. Gold occurs associated with sulfides, filling arsenopyrite fractures or free in quartz veins and gangue (Petersen, 2003).

In the CPIVESD0031 drill hole, Structure IV occurs parallel and next to the contact between the carbonaceous schist and the dolomite layer, at a depth of 850 m and approximately 6 m thick. Unlike the Palmeiras Structure, Structure IV does not exhibit such pronounced hydrothermal alteration halos since carbonaceous schist is less reactive to hydrothermal fluids. Therefore, visible hydrothermal alteration halos are strictly concentrated near the quartz vein and the mineralized zone, where textural and mineralogical variations were identified.

The carbonaceous schist is defined by a metamorphic assemblage composed of carbonaceous matter + quartz + biotite + plagioclase (andesine to oligoclase) + garnet + ilmenite ± muscovite ± chlorite ± pyrrhotite ± arsenopyrite ± chalcopyrite (Fig. 4).

The distal halo mineral assemblage is very similar to that of the unaltered host rock, indicating a low-intensity hydrothermal process with a small increase in muscovite and chlorite, and a decrease in the carbonaceous matter, biotite, and plagioclase. The sulfide phase is rare and composed of pyrrhotite and chalcopyrite. Plagioclase composition changes from andesine to oligoclase towards the proximal halo (Fig. 4).

The intermediate halo presents more evidence of hydrothermal activity and is characterized by the increase in Fe-dolomite, quartz, and muscovite contents, indicating carbonation, silicification, and sericitization processes. Chlorite, tourmaline, carbonaceous matter, biotite, oligoclase, pyrrhotite, arsenopyrite, chalcopyrite, and ilmenite also constitute the mineral assemblage of this halo (Fig. 4). Also, the concentrations of carbonaceous material, oligoclase, and biotite decrease in this halo compared to the distal halo. Tourmaline crystals can be observed locally. The sulfide contents increase, predominantly composed of pyrrhotite, arsenopyrite, and low chalcopyrite (Fig. 4). Ca is released in the transformation of andesine to oligoclase and accommodated in the carbonate structure present in this halo.

The proximal halo is characterized by foliation obliteration, accompanied by significant mineralogical changes. This halo exhibits increased quartz, oligoclase, and tourmaline concentrations, whereas Fe-dolomite content is less expressive than in the intermediate halo

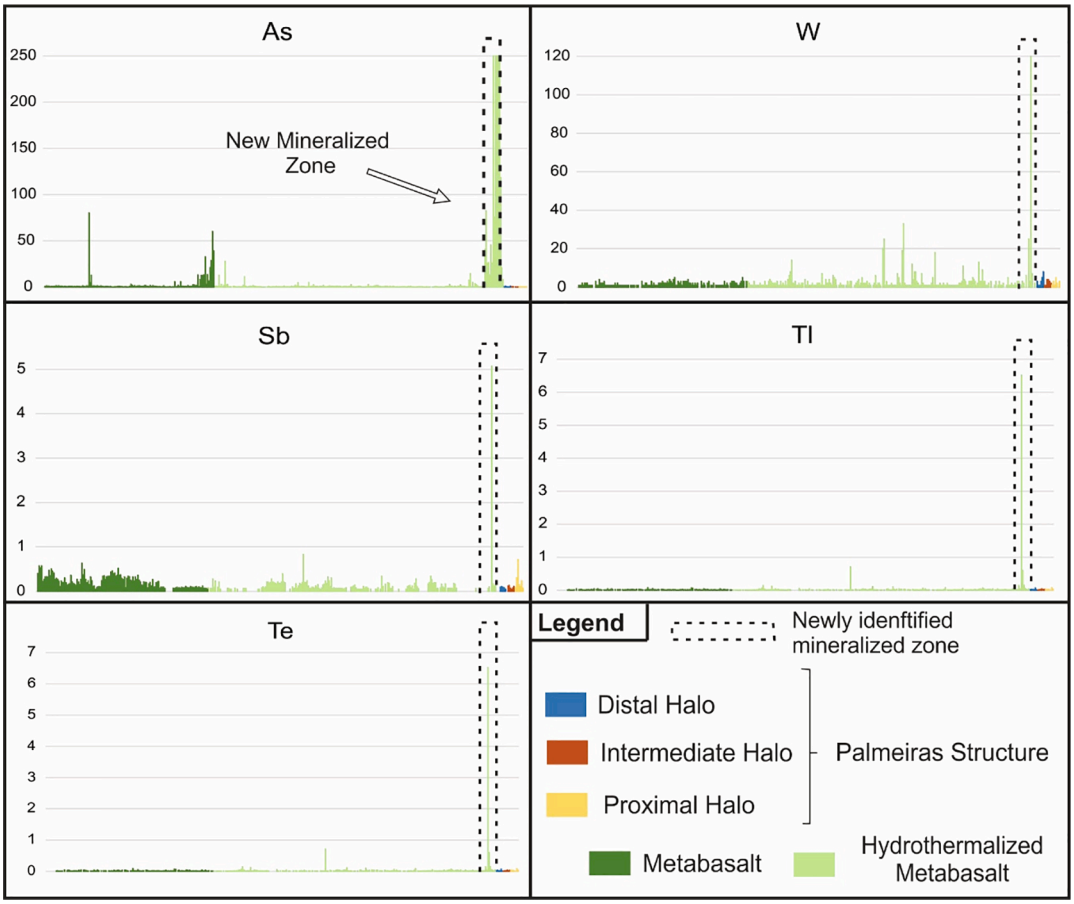

Fig. 16. Pathfinder elements distribution along the metabasalt and hydrothermally-altered metabasalt samples. Highlighted the new identified mineralized zone marked by the enrichment of As, W, Sb, Tl and Te.

(Fig. 4). Biotite, tourmaline, apatite, allanite, muscovite, rutile, arsenopyrite, pyrrhotite, and chalcopyrite also constitute the mineral assemblage of this halo. Close to the ore, there is a significant decrease in carbonaceous matter and ilmenite. In addition, sulfide content increases, marked by arsenopyrite predominance over pyrrhotite and chalcopyrite. (Fig. 4). The amount of oligoclase increases in the proximal halo relative to the intermediate halo and is recorded in the geochemical signature by the increase in Na2O contents. The content of carbonaceous material decreases progressively from the distal to the proximal halo, as a result of oxidation when interacting with hydrothermal fluids. The presence of hydrothermal oligoclase suggests hydrothermal alteration temperatures of 440° to 480° in the wall rocks (Thomson, 1991).

Although carbonaceous schists is a rock with low reflectance, the reflectance spectroscopy was efficient in vectoring Structure IV, since the hydrothermal assemblage of this mineralized zone is composed of minerals with absorption features related to VNIR-SWIR, such as muscovite, chlorite and Fe carbonate. The results prove that this is an effective tool for studying the hydrothermal footprint of Structure IV, as it allows identifying these mineral guides.

The study of the chemical element behavior in the carbonaceous schist-hosted mineralization highlighted the SiO_2, CaO, Na_2O, As, Sb, W, Te, and Re increase throughout the hydrothermal alteration halos (Fig. 17). The increase of Ca and Ba can be related to the formation of carbonate and phyllosilicates, such as biotite and muscovite. The increase in As and S concentrations reflects an increase in sulfides formation, especially arsenopyrite.

Compared to the unaltered host carbonaceous schist, the physical properties of hydrothermally altered samples do not vary significantly (Fig. 17). The average density values of 2.77, 2.774, and 2.715 g/cm^3 were determined for the distal, intermediate, and proximal halos, respectively. These values are very close to the general average density of 2,781 g/cm^3 obtained for carbonaceous schist from the CGB outside the mineralized zone. The average magnetic susceptibility values of 0.262×10^{-3}, 0.290×10^{-3}, and 0.296×10^{-3} SI, were measured for the distal, intermediate, and proximal halos, respectively, indicating no relevant changes in the rock petrophysical responses. Thus, the hydrothermal processes did not generate significant changes in the physical properties of the hydrothermal zone associated with Structure IV, although chemical and mineral changes have been identified in these zones.

Finally, Structure IV is characterized by a hydrothermal zone defined by silicification, carbonation, and sericitization, as indicated by the mineralogical and geochemical data. This data highlighted the increased SiO_2, CaO, Na2 O, K_2O, P, and Ba in the defined hydrothermal alteration halos. Enrichment in the pathfinders, such as As, W, Sb, Te, and Mo was also identified in the hydrothermal zones associated with Structure IV. It is suggested that muscovite, chlorite, and Fe dolomite can be used as mineral guides for identifying Structure IV, as highlighted in the results performed by reflectance spectroscopy (Fig. 17).

6. Conclusions

The integration of multi-source exploratory tools has been increasingly used to characterize the alteration patterns and define the footprints of mineralized zones in hydrothermal systems (Carrino et al., 2015; Naghadehi et al., 2014; Duuring et al., 2016; Simpson and Christie, 2019). The present study characterizes the records of

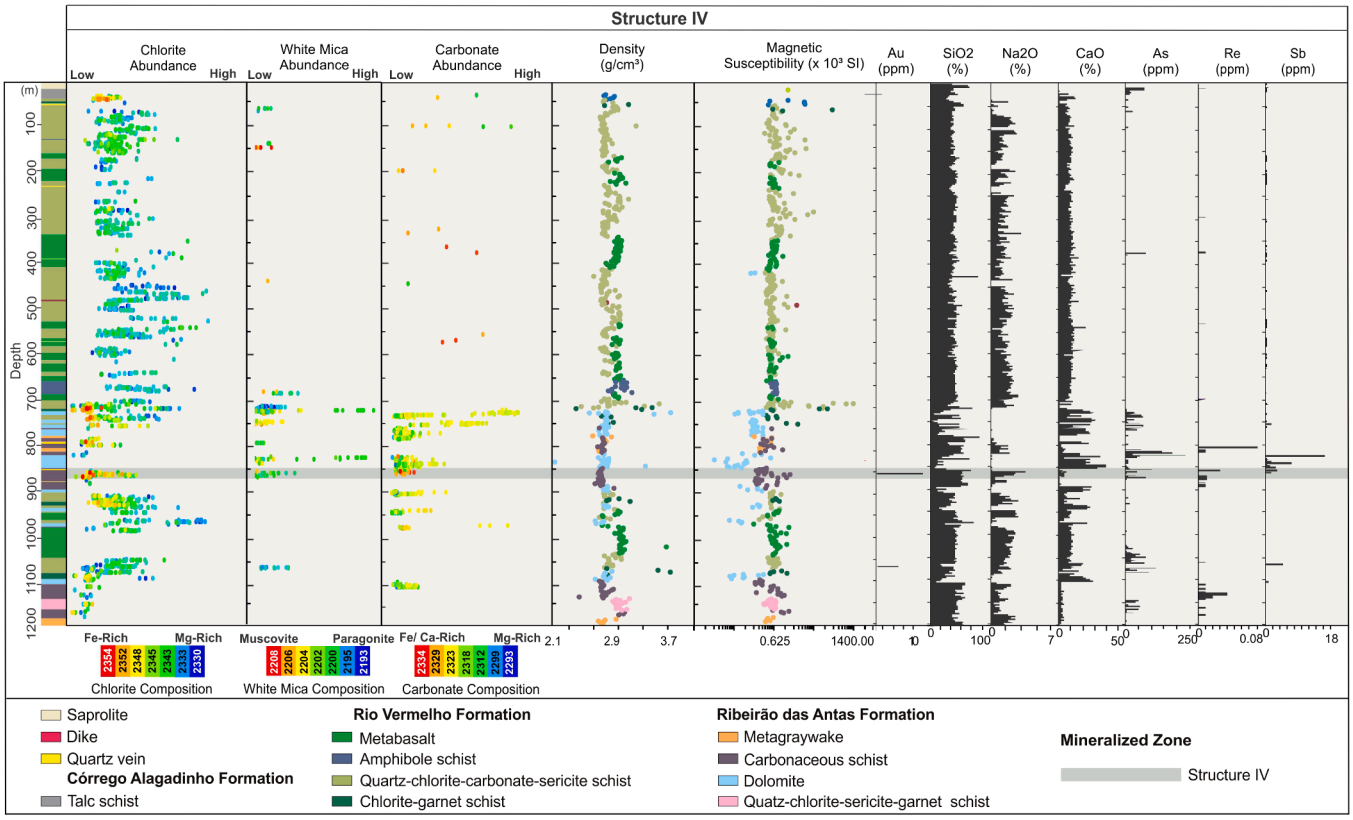

Fig. 17. Synthesis of the spectral, geochemical, and petrophysical signature of the hydrothermal alteration halos of the Structure IV.

hydrothermal processes associated with the Crixás orogenic gold deposit in two mineralized zones, one hosted in a mafic metavolcanic sequence (Palmeiras Structure) and the other hosted in a metasedimentary sequence (Structure IV). The results show that the magnitude of the hydrothermal records is different in each structure, considering that carbonaceous schists are less reactive to the hydrothermal processes than metabasalts.

The integration of the petrographical, spectral, geochemical, and petrophysical data allowed us to identify the main changes caused by the hydrothermal mineralizing processes in the rocks and define exploratory guidelines for the CGB, as indicated below:

(1) The Palmeiras Structure footprint is defined by the presence of Fe-enriched chlorite, epidote, muscovite/paragonite, alkali enrichment, as well as iron and magnetic susceptibility anomalies. A new target potential hosted in the hydrothermalized metabasalt was identified by the spectral and geochemical data. This zone signature is represented by the occurrence of muscovite, chlorite and enrichment in K2O, Ba, Rb, Li Cs and pathfinder elements such as As, W, Sb, Te. There are important vectors for metabasalt-hosted gold deposits (Table 2).

(2) The Structure IV footprint is defined by the presence of muscovite, Fe dolomite, Fe-enriched chlorite, arsenopyrite, as well as enrichment in Si, Ca, Na, and pathfinder elements such as As, W, Sb, Te, and Mo, that can predict metasedimentary-hosted gold deposits in the studied region (Table 2).

This study demonstrates that the integrated application of petrography, reflectance spectroscopy, geochemical, and petrophysical techniques is an efficient way to characterize the hydrothermal footprints of the Crixás deposit, and its results define important exploratory vectors for orogenic gold deposits in greenstone belt terranes.

Table 2
The main exploratory vectors for the Crixás gold deposit.

		Structure	
		Palmeiras	Structure IV
		Metabasalt	Carbonaceous Schist
Vectors	Mineralogical	Fe-enriched chlorite, muscovite, paragonite, epidote, and magnetite.	Arsenopyrite, Fe dolomite, Fe-enriched chlorite, and muscovite.
	Geochemical	Alkali (K, Rb, and Ba), Cs, Fe and Na enrichement.	As, W, Sb, Te, Si, Ca and, Na enrichment.
	Petrophysical	High magnetic susceptibility and high density.	

Declaration of Competing Interest

The authors declare that they have no known competing financial interests or personal relationships that could have appeared to influence the work reported in this paper.

Acknowledgements

We would like to thank the Mineração Serra Grande S.A. and their staff for providing the drill core samples and supporting the field works and analytical data acquisition. A.M. Silva and C.L.B. Toledo thank the Conselho Nacional de Desenvolvimento Científico e Tecnólogico (CNPq) for their respective research grants. This study was financed in part by the Coordenação ao de Aperfeiçoamento de Pessoal de Nível Superior – Brasil (CAPES) -Finance Code 001, by CAPES PrInt (88881.312018/2018-01) and by CNPq (Universal 420308/2018-0). The first author thanks the geologist Bruno Abilio Ciriaco for the supporting in petrographical studies and CAPES for the master's scholarship.

Appendix A. Supplementary data

Supplementary data to this article can be found online at https://doi.org/10.1016/j.oregeorev.2022.104925.

References

Airoing, M.L., Mertanen, S., 2008. Magnetic signatures related to orogenic gold mineralization, Central Lapland Greenstone Belt. Finland. Journal of Applied Geophysics 64 (1–2), 14–24.

Airo, M.-L., 2015. Geophysical signatures of mineral deposit types in Finland. Geol. Surv. Finl. 58, 9–70.

de Almeida, F.F.M., Hasui, Y., de Brito Neves, B.B., Fuck, R.A., 1981. Brazilian structural provinces: an introduction. Earth Sciences Review 17 (1-2), 1–29.

Almeida, B. Mineralização Aurífera, 2006. Alteração Hidrotermal e Indicadores Prospectivos do Corpo Palmeiras, Greenstone Belt de Crixás, Goiás. Master's Thesis, Universidade Federal do Rio Grande do Sul, Porto Alegre, Brazil.

Araújo Filho, J.O., 2000. The Pirineus Syntaxis: an example of two Brasiliano foldthrust belts in central Brazil and its implication for the tectonic evolution of western Gondwana. Revista Brasileira de Geociências 30 (2), 144–148.

Arndt, N.T., Teixeira, N.A., White, W.M., 1989. Bizarre geochemistry of komatiites from the Crixás Greenstone Belt. Contr. Mineral. Petrol. 101, 187–197.

Bacha, R.R.B., Toledo, C.L.B., Silva, A.M., Mungall, J.E., 2021. Alkali element mobility as a vector for gold mineralization: An example from Central Brazil. Geochemistry 81 (4), 125808.

Beghelli Junior, L.P., 2012. Charnockitos e ortognaisses da porção centro-oeste do Bloco Arqueano de Goiás: Dados geoquímicos e isotópicos. Master thesis, Universidade de Brasília, Brasília, 87 pp.

Bogossian, J., Hagemann, S.G., Rodrigues, V.G., Lobato, L.M., Roberts, M., 2020. Hydrothermal Alteration and Mineralization in the Faina greenstone belt: evidence from the Cascavel and Sertão orogenic gold deposits. Ore Geol. Rev. 119, 10323.

Borges, C.C.A., Toledo, C.L.B., Silva, A.M., Kirk, J., Ruiz, J., Chemale, F., Souza, R.G., Santos, B.A., Campos, M.P., Campos, L.M., Santos, A.M., 2021a. Archean to Paleoproterozoic evolution of the Crixás greenstone belt, Central Brazil: Insights from two contrasting assemblies of metaigneous rocks. Lithos 404-405, 106493.

Borges, C.C.A., Toledo, C.L.B., Silva, A.M., Chemale, F., dos Santos, B.A., Figueiredo, F.L., Zacchi, É.N.P., 2021b. Unraveling a hidden Rhyacian magmatic arc through provenance of metasedimentary rocks of the Crixás greenstone belt. Central Brazil. Precambrian Research 353, 106022.

Carrino, T.A., Crósta, A.P., Toledo, C.L.B., Silva, A.M., Silva, J.L., 2015. Geology and hydrothermal alteration of the Chapi Chiara prospect and nearby targets, southern Peru, using ASTER data and reflectance spectroscopy. Economic Geology 110 (1), 73–90.

Chang, Z., Hedenquist, J. W., White, N. C., Cooke, D. R., Roach, M., Deyell, C. L., ... & Cuison, A. L. (2011). Exploration tools for linked porphyry and epithermal deposits: Example from the Mankayan intrusion-centered Cu-Au district, Luzon, Philippines. Economic Geology, 106(8), 1365-1398.

Chopping, R., van der Wielen, S.E., 2011. Mapping the footprint of ore deposits in 3D using geophysical data. AusGeo News 101, 3–7.

Clark, R.N., King, T.V.V., Klejwa, M., Swayze, G.A., Vergo, N., 1990. High spectral resolution reflectance spectroscopy of minerals. J. Geophys. Res. 95 (B8), 12653.

Clark, R.N., 1999. Spectroscopy of rocks and minerals and principles of spectroscopy. In: Rencz, A.N. (Ed.), Remote Sensing for the Earth Sciences: manual of remote sensing, third ed., vol. 3. John Wiley and Sons, New York, pp. 3–58.

Christie, A.B., Brathwaite, R.L., 2003. Hydrothermal alteration in metasedimentary rock-hosted orogenic gold deposits, Reefton goldfield, South Island. New Zealand. Mineralium deposita 38 (1), 87–107.

de Oliveira Cordeiro, P.F., de Oliveira, C.G., 2017. The Goiás Massif: Implications for a pre-Columbia 2.2–2.0 Ga continent-wide amalgamation cycle in central Brazil. Precambrian Research 298, 403–420.

Della Giustina, M.E.S., de Oliveira, C.G., Pimentel, M.M., Buhn, B., 2009. Neoproterozoic magmatism and high-grade metamorphism in the Goiás Massif: new LA-MC-ICMPS U-Pb and Sm-Nd data and implications for collisional history of the Brasília Belt. Precambrian Research 172 (1-2), 67–79.

Danni, J. C. M., & Ribeiro, C. C., 1978. Caracterização estratigráfica da seqüência vulcano-sedimentar de Pilar de Goiás e de Guarinos, Goiás. In: SBG, Congresso Brasileiro de Geologia, 30, Recife, Anais, vol. 2, pp. 582-596.

Dentith, M., Mudge, T.S., 2014. Geophysics for the Mineral Exploration Geoscientist. Cambridge University Press, London, p. 454.

Dentith, M., Enkin, R.J., Morris, W., Adams, C., Bourne, B., 2020. Petrophysics and mineral exploration: a workflow for data analysis and a new interpretation framework. Geophysical Prospecting 68 (1), 178–199.

Dubé, B. E. N. O. Î. T., & Gosselin, P. A. T. R. I. C. E., 2007. Greenstone-hosted quartz-carbonate vein deposits. Mineral Deposits of Canada: A synthesis of major deposit-types, district metallogeny, the evolution of geological provinces, and exploration methods: Geological Association of Canada, Mineral Deposits Division, Special Publication, 5, 49-73.

Ducart, D.F., Crósta, A.P., Filho, C.R.S., Coniglio, J., 2006. Alteration mineralogy at the Cerro La Mina epithermal prospect, Patagonia, Argentina: Field mapping, short-wave infrared spectroscopy, and ASTER images. Economic Geology. 101 (5), 981–996.

Duuring, P., Hassan, L., Zelic, M., Gessner, K., 2016. Geochemical and spectral footprint of metamorphosed and deformed VMS-style mineralization in the Quinns district, Yilgarn Craton. Western Australia. Economic Geology 111 (6), 1411–1438.

Eilu, P., Mikucki, E.J., 1998. Alteration and primary geochemical dispersion associated with the Bulletin lode-gold deposit, Wiluna, Western Australia. Journal of Geochemical Exploration 63 (2), 73–103.

Eilu, P., Mikucki, E.J., Dugdale, A.L., 2001. Alteration zoning and primary geochemical dispersion at the Bronzewing lode-gold deposit. Western Australia. Mineralium Deposita 36 (1), 13–31.

Ferreira Filho, C.F., Kamo, S.L., Fuck, R.A., Krogh, T.E., Naldrett, A.J., 1994. Zircon and rutile U-Pb geochronology of the Niquelândia layered mafic and ultramafic intrusion, Brazil: constraints for the timing of magmatism and high grade metamorphism. Precambrian Research 68 (3–4), 241–255.

Ferreira Filho, C.F., De Moraes, R., Fawcett, J.J., Naldrett, A.J., 1998. Amphibolite to granulite progressive metamorphism in the Niquelândia Complex, central Brazil: regional tectonic implications. Journal of South American Earth Sciences 11 (1), 35–50.

Fortes, P.T.F.O., 1996. Metalogênese dos depósitos auríferos Mina III, Mina Nova e Mina Inglesa, greenstone belt de Crixás, GO. PhD thesis, Universidade de Brasília, 176 pp.

Fortes, P.T.F.O., Cheilletz, A., Giuliani, G., Feraud, G., 1997. A Brasiliano age (500 ±5 Ma) for the Mina III gold deposit, Crixás greenstone belt, Goiás state, central Brazil. International Geology Review 39, 449–460.

Fortes, P.T.F.O., Pimentel, M.M., Santos, R.V., Junges, S., 2003. Sm-Nd study of the Crixás Greenstone Belt, Brazil: implications for the age of deposition of the upper sedimentary rocks and associated Au mineralization. Journal of South American Earth Sciences 16, 503–512.

Gaffey, S.J., 1986. Spectral reflectance of carbonate minerals in the visible and near-infrared (0.35-2.55 microns); calcite, aragonite, and dolomite. American Mineralogist 71 (1–2), 151–162.

Gaillard, N., Williams-Jones, A.E., Clark, J.R., Salvi, S., Perrouty, S., Linnen, R.L., Olivo, G.R., 2020. The use of lithogeochemistry in delineating hydrothermal fluid pathways and vectoring towards gold mineralization in the Malartic district. Québec. Ore Geology Reviews 120, 103351.

Goldfarb, R.J., Baker, T., Dubé, B., Groves, D.I., Hart, C.J.R., Gosselin, P., 2005. Distribution, character, and genesis of gold deposits in metamorphic terranes. Economic Geology 100th anniversary volume, 407–450.

Groves, D.I., Goldfarb, R.J., Gebre-Mariam, M., Hagemann, S.G., Robert, F., 1998. Orogenic gold deposits: A proposed classification in the context of their crustal distribution and relationship to other gold deposit types. Ore Geol. Rev. 13 (1-5), 7–27.

Harraden, C.L., Mcnulty, B.A., Gregory, M.J., Lang, J.R., 2013. Shortwave infrared spectral analysis of hydrothermal alteration associated with the Pebble porphyry copper-gold-molybdenum deposit, Iliamna. Alaska. Economic Geology. 108 (3), 483–494.

Heath, C.J., Campbell, I.H., 2004. A New Geochemical Technique for Gold Exploration: Alkali Element Mobility Associated with Gold Mineralization in the West Australian Goldfields. Economic geology 99, 313–324.

Hunt, G.R., Salisbury, J.W., 1971. Visible and near-infrared spectra of minerals and rocks. II. Carbonates. Modern Geology 2, 23–30.

Hunt, G.R., 1977. Spectral signatures of particulate minerals in the visible and near-infrared. Geophysics. 42 (3), 501–513.

Jost, H., De Oliveira, A.M., 1991. Stratigraphy of the greenstone belts, Crixás region, Goiás, Central Brazil. Journal of South American Earth Sciences 4 (3), 201–214.

Jost, HARDY, Fuck, REINHARDT, Brod, JOSÉ.A., Dantas, E.L., Meneses, P.R., Assad, M.L. L., Pimentel, MÁRCIO.M., Blum, M.DE.L.B., Silva, A.M., Spigolon, ANDRÉ.L.D., Maas, M.V.R., Souza, M.M.DE., Fernandez, B.P., Faulstich, F.R.L., Macedo júnior, P. M.DE., Schobbenhaus, C.N., Almeida, L.DE., Silva, A.A.C.DA., Anjos, C.W.D.D., Santos, A.P.M.R., Bubenick, ANDRÉ.N., Teixeira, A.DE.A., Lima, B.EUSTÁQUIO.M., Campos, M.DE.O., Barjud, R.M., Carvalho, D.R.DE., Scislewski, L.R., Sarli, CLÁUDIO. L., Oliveira, D.P.L.DE., 2001. Geologia de terrenos Arqueanos e Proterozóicos da região de Crixás-Cedrolina. Goiás. Revista Brasileira de Geociências 31 (3), 315–328.

Jost, H., de Oliveira, P.D.T.F., 2001. Gold deposits and occurrences of the Crixás Goldfield, central Brazil. Mineralium Deposita 36 (3–4), 358–376.

Jost, H., Dussin, I.A., Chemale Jr., F., Tassinari, C.C.G., Junges, S., 2008. U-Pb and Sm-Nd constraints for the Paleoproterozoic age of the metasedimentary sequences of the Goiás Archean greenstone belts. South Am. Symp. Isotope Geology, 6, San Carlos de Bariloche, Argentina, Proceedings, 4 pp.

Jost, H., Theodoro, S.M.C.H., Figueiredo, A.M.G., Boaventura, G.R., 1996. Propriedades geoquímicas e proveniência de rochas metassedimentares detríticas arqueanas dos greenstone belts de Crixás e Guarinos, Goiás. Revista Brasileira de Geociências 26, 151–166.

Jost, H., Chemale, F., Dussin, I.A., Tassinari, C.C.G., Martins, R., 2010. A U-Pb zircon Paleoproterozoic age for the metasedimentary host rocks and gold mineralization of the Crixás greenstone belt, Goiás. Central Brazil. Ore Geol. Reviews 37 (2), 127–139.

Jost, H., Chemale Jr., F., Fuck, R.A., Dussin, R.A., 2013. Uvá complex, the oldest orthogneisses of the Archean Paleoproterozoic terrane of central Brazil. Journal of South American Earth Sciences 47, 201–212.

Jost, H., Carvalho, M.J., Rodrigues, V.G., Martins, R., 2014. Metalogênese dos greenstone belts de Goiás. In: Silva, M.G., Neto, M.B.R., Jost, H., Kuyumjian, R.M. (Orgs.), Metalogênese das províncias tectônicas brasileiras, Belo Horizonte, CPRM, pp. 141-168.

Jost, H., Hofmann Apollo, J.F., Weber, W., Salles, R.D.R., Marques, J.C., Massucatto, A. J., Costa, D.A., Araújo dos Santos, B., 2019. Stratigraphic update, paleotectonic, paleogeographic, and depositional environments of the Crixás Greenstone Belt, Central Brazil. Journal of South American Earth Sciences 96, 102329.

King, T.V., Clark, R.N., 1989. Spectral characteristics of chlorites and Mg-serpentines using high-resolution reflectance spectroscopy. Journal of Geophysical Research: Solid Earth 94 (B10), 13997–14008.

Kishida, A., Kerrich, R., 1987. Hydrothermal alteration zoning and gold concentration at the Kerr-Addison Archean lode gold deposit, Kirkland Lake. Ontario. Economic Geology 82 (3), 649–690.
Kuyumjian, R.M., 1981. Geologia e mineralizações auríferas do greenstone belt da faixa Crixás, GO. Universidade de Brasília, p. 69. Master thesis.
Lypaczewski, P., Rivard, B., 2018. Estimating the Mg# and AlVI content of biotite and chlorite from shortwave infrared reflectance spectroscopy: Predictive equations and recommendations for their use. International journal of applied earth observation and geoinformation 68, 116–126.
Large, R.R., Bull, S.W., McGoldrick, P.J., 2000. Lithogeochemical halos and geochemical vectors to stratiform sediment hosted Zn–Pb–Ag deposits: part 2. HYC deposit, McArthur River, Northern Territory. Journal of Geochemical Exploration 68 (1–2), 105–126.
Liebscher, A., 2004. Spectroscopy of epidote minerals. Reviews in Mineralogy and Geochemistry 56 (1), 125–170.
Magalhães, L.F., 1991. Cinturão de cisalhamento de empurrão Córrego Geral/Meia Pataca: geologia, deformação, alteração hidrotermal e mineralizações auríferas associadas (Crixás, Goiás). Universidade de Brasília, p. 233. Master thesis.
Marques, J. C., Jost, H., Creaser, R. A., Frantz, J. C., Osorio, R. G., 2013. Age of arsenopyrite gold-bearing massive lenses of the Mina III and its implications on exploration, Crixás greenstone belt, Goiás, Brazil. In: III Simpósio Brasileiro de Metalogenia, Gramado, extended abstracts.
Massucato, A.J., 2004. Relatório de Geologia Estrutural - Aspectos Estruturais do GreenstoneBelt de Crixás - GO – AngloGold Ashanti, Crixás-GO, Internal Report.
McLeod, R.L., Gabell, A.R., Green, A.A., Gardavsky, V., 1987. Chlorite infrared spectral data as proximity indicators of volcanogenic massive sulfide mineralization. In: Proceedings of Pacific Rim Congress, pp. 321–324.
Melzer, S., Wunder, B., 1999. Experimentally determined K-Rb-Cs exchange coefficients between micas, amphiboles, and aqueous chloride solutions between 0.2 and 4 GPa. Eos (Transactions, American Geophysical Union) 80, 361.
Naghadehi, K.M., Hezarkhani, A., Asadzadeh, S., 2014. Mapping the alteration footprint and structural control of Taknar IOCG deposit in east of Iran, using ASTER satellite data. International Journal of Applied Earth Observation and Geoinformation 33, 57–66.
Petersen Jr., K.J., 2003. Estudo das mineralizações auríferas do Corpo IV e V da Estrutura IV do greenstone belt de Crixás (GO). PhD thesis. Universidade de São Paulo, 195p.
Phillips, G.N., Powell, R., 2010. Formation of gold deposits: a metamorphic devolatilization model. J. Metamorph. Geol. 28, 689–718.
Prado, E.M.G., Silva, A.M., Ducart, D.F., Toledo, C.L.B., de Assis, L.M., 2016. Reflectance spectroradiometry applied to a semi-quantitative analysis of the mineralogy of the N4ws deposit, Carajás Mineral Province, Pará, Brazil. Ore Geology Reviews 78, 101–119.
Pirajno, F. (Ed.), 2009. Hydrothermal Processes and Mineral Systems. Springer Science & Business Media.
Pimentel, M.M., Fuck, R.A., 1992. Neoproterozoic crustal accretion in Central Brazil. Nature 20 (4), 375–379.
Pimentel, M.M., Fuck, R.A., Jost, H., Ferreira Filho, C.F., Araújo, S.M., 2000. In: Cordani, U.G., Milani, E.J., Thomaz Filho, A., Campos, D.A. (Eds.), Tectonic Evolution of South America. Rio de Janeiro, 31st International Geological Congress. , pp. 151–182.
Pimentel, M.M., Jost, H., Fuck, R.A., 2004a. O embasamento da Faixa Brasília e o Arco Magmático de Goiás. In: Mantesso-Neto, V., Bartorelli, A., Carneiro, C.D.R., Neves, B. B.B. (Eds.), Geologia do Continente Sul-Americano: evolução da obra de Fernando Fávio Marques de Almeida. Beca Produções Culturais Ltda, São Paulo, pp. 356–368.
Pimentel, M.M., Filho, C.F.F., Armstrong, R.A., 2004b. SHRIMP U-Pb and Sm-Nd ages of the Niquelândia layered complex: Meso-(1.25 Ga) and Neoproterozoic(0.79 Ga) extensional events in central Brazil. Precambrian Research 132 (1-2), 133–153.
Piuzana, D., Pimentel, M.M., Fuck, R.A., Armstrong, R., 2003. SHRIMP U-Pb and Sm-Nd data for the Araxá Group and associated rocks: Constraints for the age of sedimentation and geodynamic context of the southern Brasília Belt, central Brazil. Precambrian Research 125, 139–160.
Post, J.L., Noble, P.N., 1993. The near-infrared combination band frequencies of dioctahedral smectites, micas, and illites. Clays and clay minerals 41 (6), 639–644.
Queiroz C.L. 1995. Caracterização dos domínios estruturais e da arquitetura do greenstone belt de Crixás, Go. Master thesis, Universidade de Brasília, 119 pg.
Queiroz, C.L., Jost, H., da Silva, L.C., McNaughton, N.J., 2008. U-Pb SHRIMP and Sm–Nd geochronology of granite–gneiss complexes and implications for the evolution of the Central Brazil Archean Terrain. Journal of South American Earth Sciences 26 (1), 100–124.
Resende, M.G., Jost, H., Osborne, G.A., Mol, A.G., 1998. Stratigraphy of the Goiás and Faina greenstone belts, Central Brazil: a new proposal. Revista Brasileira de Geologia 28, 77–94.
Sabóia, L.A., Teixeira, N.A., 1983. Ultramaphic flows of the Crixás greenstone belt. Goiás. Precambrian Research. 22, 23–40.
Seer, H.J., Brod, J.A., Fuck, R.A., Pimentel, M.M., Boaventura, G.R., Dardenne, M.A., 2001. Grupo Araxá em sua área tipo: um fragmento de crosta oceânica neoproterozóica na Faixa de Dobramentos Brasília. Revista Brasileira de Geociências 31 (3), 385–396.
Simpson, M.P., Christie, A.B., 2019. Hydrothermal alteration mineralogical footprints for New Zealand epithermal Au-Ag deposits. New Zealand Journal of Geology and Geophysics 62 (4), 483–512.
Sobiesiak, M.S. 2011. Caracterização de depósito aurífero no Corpo Pequizão, Crixás-GO. Trabalho de Conclusão de Curso de Geologia, Instituto de Geociências, Universidade Federal do Rio Grande do Sul.
Souza, R. G. D. 2018. Caracterização do Corpo aurífero Mangaba, Estrutura IV, Greenstone Belt de Crixás-GO. Trabalho de Conclusão de Curso de Geologia, Instituto de Geociências, Universidade Federal do Rio Grande do Sul.
Strieder, A.J., Nilson, A.A., 1992. Mélange ofiolítica nos metassedimentos do Grupo Araxá de Abadiânia (GO) e implicações tectônicas regionais. Revista Brasileira de Geociências 22, 204–215.
Tassinari, C.C.G., Jost, H., Santos, J.C., Nutman, A.P., Bennell, M.R., 2006. Pb and Nd isotope signatures and SHRIMP U-Pb geochronological evidence of Paleoproterozoic age for Mina III gold mineralization. In: 5 o SSAGI South American Symposium on Isotope Geology, Pucon, Chile, Proceedings, 615-617.
Thomson, M.L., 1987. The Crixás gold deposit, Brazil: metamorphism, metasomatism and gold mineralization. Ph.D. Thesis, Univ. Western Ontario, Ontario, Canada. 345pp.
Thomson, M.L., Fyfe, W.S., 1990. The Crixás gold deposit, Brazil; thrust-related, postpeak metamorphic gold mineralization of possible Brasilino Cycle age. Economic Geology 85 (5), 928–942.
Thomson, M., 1991. Wall-rock alteration related to Au mineralization in the low amphibolite facies; Crixás gold mine, Goias. Brazil. Can. Mineral 29, 461–480.
Tian, J., Zhang, Y., Cheng, J.M., Sun, S.Q., Zhao, Y.J., 2019. Short wavelength infra-red (SWIR) characteristics of hydrothermal alteration minerals in skarn deposits: example from the Jiguanzui Cu–Au deposit, Eastern China. Ore Geology Reviews 106, 134–149.
Ulrich, S., Hageman, S., Marques, J.C., Figueiredo, F.L.A., Ramires, J.E., Frantz, J.C., Petersen, K., 2021. The Orogenic Crixás Gold Deposit, Goiás, Brazil: A Review and New Constraints on the Structural Control of Ore Bodies. Minerals 11 (10), 1050.
Valeriano, C.M., Pimentel, M.M., Heilbron, M., Almeida, J.C.H., Trouw, R.A.J.,2008. Tectonic evolution of the Brasilia Belt, central Brazil, and Early Assembly of Gondwana. Vol. 294. Geological Society, London, Special Publications, pp. 197-210.
Van Der Meer, Freek, 2004. Analysis of spectral absorption features in hyperspectral imagery. International journal of applied earth observation and geoinformation 5, 55–68.
Vedder, W., McDonald, R., 1963. Vibrations of the OH ions in muscovite. The Journal of Chemical Physics. 38, 1583–1590.
Xu, Y., 1999. The stable isotope and trace element geochemistry of the Victory gold deposit. Australian National University, Western Australia. Ph.D. thesis.
Yamaoka, W.N., & Araújo, E.M., 1988. Depósitos de Ouro Mina III, Crixás, Goiás. In: C. Schobbenhaus & C.E.S. Coelho (Eds.). Principais Depósitos Minerais do Brasil, Brasília, NPM/CVRD, v. 3, cap. 34, p. 491-498.
Yang, K., Lian, C., Huntington, J.F., Peng, Q., Wang, Q., 2005. Infrared spectral reflectance characterization of the hydrothermal alteration at the Tuwu Cu-Au deposit, Xinjiang. China. Miner. Depos. 40 (3), 324–336.
Zhang, S., Chu, G., Cheng, J., Zhang, Y.u., Tian, J., Li, J., Sun, S., Wei, K., 2020a. Short wavelength infrared (SWIR) spectroscopy of phyllosilicate minerals from the Tonglushan Cu-Au-Fe deposit, Eastern China: New exploration indicators for concealed skarn orebodies. Ore Geology Reviews 122, 103516.
Zhang, S., Xiao, B., Long, X., Chu, G., Cheng, J., Zhang, Y.u., Tian, J., Xu, G., 2020b. Chlorite as an exploration indicator for concealed skarn mineralization: Perspective from the Tonglushan Cu–Au–Fe skarn deposit. Ore Geology Reviews 126, 103778.

Further reading

da Silva, G.F., Ferreira, M.V., Costa, I.S.L., Bernardes, R.B., Mota, C.E.M., Jiménez, F.A. C., 2021. Qmin–A machine learning-based application for processing and analysis of mineral chemistry data. Computers & Geosciences 157, 104949.
Deer, W. A., Howie, R. A., & Zussman, J. (Eds.). (1997). Rock-forming minerals: disilicates and ring silicates, volume 1B. Geological Society of London.
Hamisi, J., MacKenzie, D., Pitcairn, I., Blakemore, H., Zack, T., Craw, D., 2017. Hydrothermal footprint of the Birthday reef, Reefton goldfield, New Zealand. New Zealand Journal of Geology and Geophysics 60 (2), 59–72.
Hey, M.H., 1954. A new review of the chlorites. Mineralogical magazine and journal of the Mineralogical Society 30 (224), 277–292.
Leake, B.E., Woolley, A.R., Arps, C.E.S., Birch, W.D., Gilbert, M.C., Grice, J.D., Hawthorne, F.C., Kato, A., Kisch, H.J., Krivovichev, V.G., Linthout, K., Laird, J., Mandarino, J., Maresch, W.V., Nickel, E.H., Rock, N.M.S., Schumacher, J.C., Smith, D.C., Stephenson, N.C.N., Ungaretti, L., Whittaker, E.J.W., Youzhi, G., 1997. Nomenclature of amphiboles; report of the Subcommittee on Amphiboles of the International Mineralogical Association Commission on new minerals and mineral names. Mineralogical magazine 61 (405), 295–310.
Tischendorf, G., Förster, H.J., Gottesmann, B., Rieder, M., 2007. True and brittle micas: composition and solid-solution series. Mineralogical Magazine 71 (3), 285–320.